Langmuir

The ACS Journal of Surfaces and Colloids

NOVEMBER 6, 2012
VOLUME 28, NUMBER 44
pubs.acs.org/Langmuir

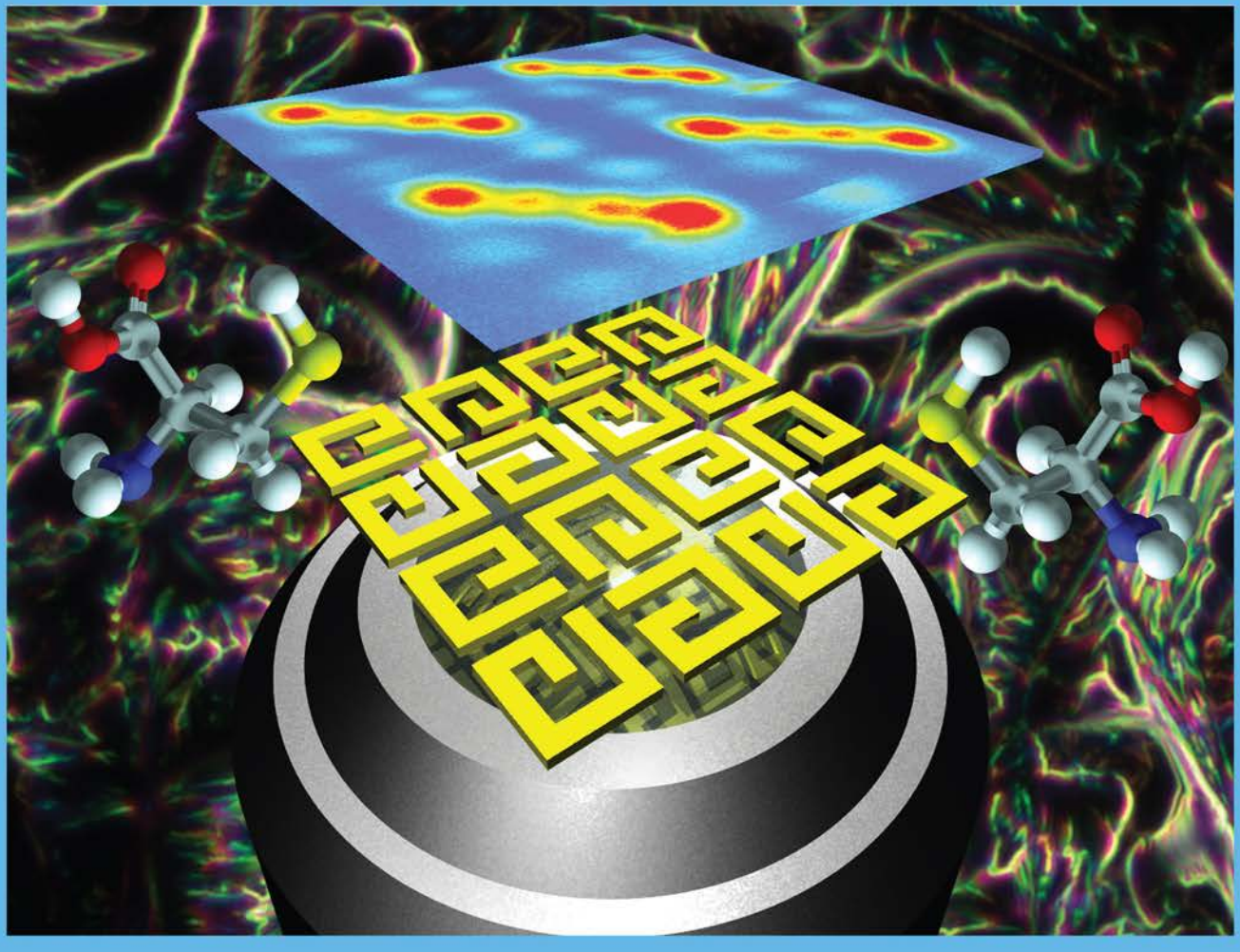

Second Harmonic Generation Microscopy from Chiral G-Shaped Nanostructures Made of Gold

(see p. 5A)

ACS Publications
MOST TRUSTED. MOST CITED. MOST READ.

www.acs.org

Langmuir

Invited Feature Article

pubs.acs.org/Langmuir

Characterization of Nanostructured Plasmonic Surfaces with Second Harmonic Generation

V. K. Valev*,†

Molecular Imaging and Photonics, KU Leuven, Celestijnenlaan 200 D, B-3001 Leuven, Belgium

ABSTRACT: Because of its high surface and interface sensitivity, the nonlinear optical technique of second harmonic generation (SHG) is a designated method for investigating nanostructured metal surfaces. Indeed, the latter present a high surface-to-volume ratio, but even more importantly, they can exhibit strong near-field enhancements or "hot spots". Hot spots often appear as a result of geometric features on the nanoscale or surface plasmon resonances, which are collective electron oscillations on the surface that, on the nanoscale, can readily be excited by light. In the last 10 years, near-field hot spots have been responsible for dramatic developments in the field of nano-optics. In this Feature Article, the influence of hot spots on the SHG response of nanostructured metal surfaces is discussed on both the microscopic and macroscopic levels. On the microscopic level, the nanostructured metal surfaces were characterized by scanning SHG microscopy, complemented by rigorous numerical simulations of the near-field and of the local electric currents at the fundamental frequency. On the macroscopic level, SHG-circular dichroism and magnetization-induced SHG characterization techniques were employed.

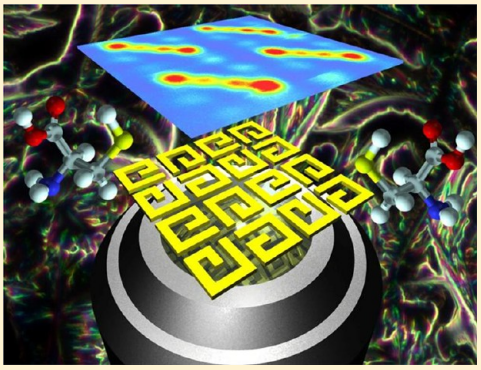

1. INTRODUCTION

Nowadays, second harmonic generation[1] (SHG) has become a widespread technology, mostly in the form of green laser pointer light. Indeed, these pointers contain a diode laser that emits light at the near-infrared wavelength of 1064 nm, which is then converted to 532 nm green light by a frequency-doubling crystal. To function, such crystals need to fulfill very restrictive requirements; for instance, they must have the same refractive index at both the fundamental and the second harmonic light frequency. Light propagating through the crystal can give rise to SHG along its entire length of propagation. However, unless all of this second harmonic light propagates in phase, it will interfere destructively with itself and will cancel out. This is called the phase-matching condition, and it is so restrictive that very few bulk materials can achieve optical SHG. Contrary to bulk materials, though, all material surfaces are SHG-active. Unfortunately, conversion efficiencies for surface SHG in metals are on the order of 10^{-14}. However, this factor can be significantly improved upon nanostructuring the metal surfaces, thereby enabling very high near-field enhancements. Moreover, it is possible to concentrate the near-field enhancements in the gaps between the nanostructures, where embedding strongly nonlinear materials can ensure an additional enlargement of the frequency conversion. Although significant effort has thus been devoted to enlarging the SHG signal from nanostructured interfaces, it should be noted that the importance of surface SHG extends well beyond a mere frequency conversion factor.

Understanding the surface sensitivity of SHG is very intuitive because, by definition, the surface breaks the symmetry of the material. More generally, within the dipole approximation, the SHG process is allowed in all materials that lack a center of symmetry (i.e., the noncentrosymmetric materials, those where changing the sign of the Cartesian coordinates affects the material). For instance, centrosymmetry is broken at the surfaces and interfaces of materials, which allows SHG to be surface/interface-sensitive down to the atomic monolayer.[2] Additionally, centrosymmetry can be broken by externally applied electric[3] or magnetic[4] dc fields, though in the case of the latter interpreting the results might require a degree of caution.[5] This type of field sensitivity allows SHG to image ferroelectric[6] and ferromagnetic[7] domains successfully. Moreover, the centrosymmetry is broken by chirality—the handedness of nature. Consequently, second harmonic equivalents of optical rotatory dispersion (ORD) and circular dichroism (CD) have been observed and are designated as SHG-ORD[8] and SHG-CD,[9] respectively. These nonlinear equivalents are typically several orders of magnitude more sensitive than their linear counterparts; consequently, SHG is successfully employed for the study of chemistry, pharmacology, and biology, where the chirality of the organic molecules plays an important role. More generally, even if the molecules are not chiral, their ordering can break the centrosymmetry. It follows that SHG is successfully employed to probe the growth of molecular monolayers, the layer-by-layer growth of molecular films, and the orientation and supramolecular ordering of adsorbed molecules. Recently, much interest has been devoted to the case where molecules are adsorbed on the surfaces of

Received: June 19, 2012
Revised: August 13, 2012
Published: August 14, 2012

dx.doi.org/10.1021/la302485c | *Langmuir* 2012, 28, 15454−15471

nanostructured metal films, which exhibit very inhomogeneous optical near-fields.

1.1. "Hot Spots" in the Optical Near-Field. Let us consider the electric field in the vicinity of a nanostructured metal surface that is illuminated by visible light from the point of view of approaching molecules. Far from the surface, these molecules would experience the electric field of light itself, which can be incident from the source, reflected from the metal surface and scattered, or diffracted, from the nanostructures. Close to the metal surface, the electromagnetic oscillations of light drive the electron density within the nanostructures, and in turn these variations in electron density constitute the source of a very inhomogeneous surface electric field—the near-field.[10] Because of its inhomogeneity, molecules placed in the near-field are subjected to electric forces with varying strengths and directions. If we were to connect all of the molecules and nanostructures, with imaginary lines drawn along the direction of these electric forces, we would obtain an image of the electric field lines. This visualization would show that the electric field lines become very concentrated in certain regions on the metal surface—the regions of near-field enhancement or "hot spots". Hot spots can occur at the corners and tips of nanostructures because of the geometric confinement of the field lines. This confinement is referred to as "the electrostatic lighting rod effect", with its physical principle being similar to that of St. Elmo's fire at the tip of a lightning rod. Another main reason for the occurrence of near-field hot spots is the surface plasmon resonance phenomenon.

Surface plasmons are coherent electron oscillations that exist at the interface between two materials, where the real part of the dielectric function changes sign across the interface, for instance, a metal–dielectric interface such as a gold sheet in air (Figure 1a). On the nanoscale, these electron oscillations can be excited very efficiently with light in the visible range of the electromagnetic spectrum, and an intuitive way to visualize the process is to consider a spherical nanoparticle (Figure 1b). Indeed, in response to the electric field of light, the electron cloud of the nanoparticle oscillates at the frequency of light and can reemit light at that same frequency, providing an additional electric field source for nearby molecules.

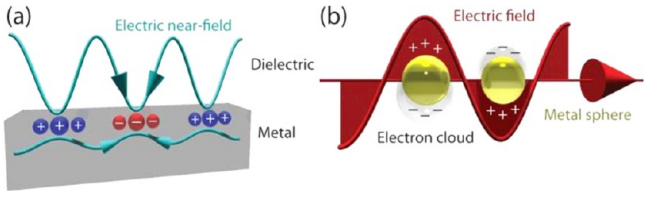

Figure 1. (a) Schematic diagram representing the surface plasmon resonance, whereby a coherent oscillation of the surface charges can occur at a metal/dielectric interface. Such surface plasmon resonances can be readily excited by the electric field of light. (b) This electric field can efficiently drive the electron cloud of a gold nanoparticle. It follows that the plasmonic waves oscillate at the frequency of the incident light.

Consequently, within hot spots, the optical response of molecules can be extremely enlarged.[11,12] A particularly spectacular example is surface-enhanced Raman scattering (SERS),[13] whereby the Raman signal can be increased by up to 14 orders of magnitude.[14,15] This enlargement is due in part to the fact that the molecules are subjected to a highly enhanced near-field, which, as it was mentioned above, is itself due to variations in the local electron density. This varying local electron density can also have an effect on the molecules via mechanisms of charge transfer, for instance, with the highest occupied molecular orbital or the lowest unoccupied molecular orbital. These charge transfers can lead to SERS or to electrochemical reactions. Thermochemical aspects can also play an important role in hot spots because the usually elevated temperature within hot spots can be a decisive factor in whether a given reaction is favorable or unfavorable; both chemical transformations[16] and catalytic reactions[17,18] have thus been reported. The near-field can also trigger photochemical reactions[19−22] and could induce two-photon photopolymerization.[23,24] The variety of chemical reactions that occur within hot spots is increasingly being used for chemical and biosensing applications.[25,26] Because such applications require the use of optical near-field enhancements at the surface, their study can greatly benefit from a surface-specific optical technique such as second harmonic generation.

1.2. Second Harmonic Generation from Spherical Metal Nanoparticles. Let us consider again the illuminated spherical metal nanoparticle in Figure 1b. The system can be modeled as a driven harmonic oscillator, where the driving force is provided by the electric field of light ($\mathbf{E}$). This field repels the electron cloud causing charge separation across the nanoparticle. The charge separation, also referred to as induced polarization, is responsible for the restoring force on the oscillating electron cloud; this is the attractive force exerted by the positively charged side of the nanoparticle. When the driving force is still in the linear regime of the restoring force, the charges oscillate linearly and the induced polarization can be written as $\mathbf{P} = \chi^{(1)}\cdot\mathbf{E}$, where the proportionality term $\chi^{(1)}$ is the linear electric susceptibility. However, upon increasing the driving force, for instance, by increasing the intensity of incident light, the charge oscillator enters the nonlinear regime. In practice, this means that the oscillating charges start exhibiting a complex motion, one that can be mathematically described as a series of higher harmonics. Henceforth, higher harmonics appear in the expression for induced polarization

$$\mathbf{P}(\omega) = \chi^{(1)}\cdot\mathbf{E}(\omega) + \chi^{(2)}\colon \mathbf{E}(\omega)\,\mathbf{E}(\omega) + \chi^{(3)}\vdots\mathbf{E}(\omega)\,\mathbf{E}(\omega)\,\mathbf{E}(\omega) + \ldots \quad (1)$$

where $\chi^{(2)}$ and $\chi^{(3)}$ are nonlinear susceptibilities associated with the emission of second and third harmonic light, respectively. Because the second harmonic term is the first of the nonlinear harmonics, it is often the largest nonlinear optical contribution. Nevertheless, second harmonic emission usually requires considerable light intensity, which is why it was demonstrated only after the invention of the laser. It is very straightforward to see how the two associated electric field terms at the fundamental frequency produce an induced polarization at the second harmonic frequency. Simply consider that for plane waves the time dependence is often represented by complex exponential functions plus complex conjugate terms. The second harmonic then appears as a consequence of $e^{i\omega t}e^{i\omega t} = e^{i(2\omega)t}$. Although the high light intensity is a necessary condition for the SHG process, it is not a sufficient condition.

Let us consider the effect of inversion symmetry on the induced polarization at the second harmonic

$$P_i(2\omega) = \chi^{(2)}_{ijk}\colon E_j(\omega)\,E_k(\omega) \quad (2)$$

dx.doi.org/10.1021/la302485c | Langmuir 2012, 28, 15454−15471

where ω is the frequency of incident light and i, j, and k are the Cartesian indices. Under inversion symmetry, all Cartesian indices change their sign; therefore, all vectors in eq 2 change their sign. It follows that

$$-P_i(2\omega) = \chi^{(2)}_{ijk} : (-E_j(\omega))(-E_k(\omega)) = P_i(2\omega) = 0 \quad (3)$$

which means that, within the dipole approximation, second harmonic light is forbidden in all materials where inversion symmetry can be applied (i.e., the centrosymmetric materials). In fact, one of the best examples of a centrosymmetric material is a spherical gold nanoparticle.

Gold has a face-centered-cubic crystal structure, which means that it is centrosymmetric. Moreover, the spherical shape of the nanoparticle is also centrosymmetric. It follows that, in the absence of externally applied electric or magnetic fields, the canonical example of plasmon local field enhancements should not give rise to any second harmonic signal. However, experimentally it has been demonstrated that surface plasmon resonances do give rise to an enhanced second harmonic signal.[27] Additionally, a strong second harmonic signal was observed from 4 nm large gold clusters,[28] from gold colloids with sizes ranging from 5 to 22 nm,[29] from gold nanoparticles with an 11 nm diameter,[30] and from silver nanoparticles with a 40 nm diameter.[31] Interestingly, in the latter work, polarization measurements demonstrated that, although forbidden in the dipole approximation, the second harmonic signal is precisely of dipolar origin.

The "forbidden" signal can be explained by small deviations in shape from the centrosymmetry of the nanoparticles. This process of dipolar SHG is in fact quite general because such symmetry deviations at the surface can also be observed in nanorods[32] and nanodecahedra.[33] In fact, the latter investigation went further and compared the SHG signal with that of spherical nanoparticles as a function of size, within the range 17 to 150 nm. It was shown that above 50 nm, spherical and decahedral nanostructures exhibit similar SHG behavior, which indicates a common origin, namely, multipolar contributions and retardation effects. However, below 50 nm, the SHG signal was clearly of dipolar origin. Please note that here the term "multipolar" is not employed in the context of Mie theory, where it designates multipolar plasmon modes. Instead, multipolar refers to nonlinear sources, such as bulk currents. The contribution of these bulk-specific nonlinear sources naturally increases with the size of the nanoparticles. Indeed, the idea that different SHG mechanisms are at work depending on the size of the plasmonic nanoparticles was also experimentally confirmed upon studying gold nanoparticles within the range of 10 to 150 nm[34,35] and silver nanoparticles within the range of 20 to 80 nm.[36] A theoretical model based on phenomenological parameters was also proposed to account for this size dependence.[37]

To summarize, for smaller gold nanoparticles the SHG signal is of dipolar origin and originates from the (nonperfectly spherical) surface of the nanoparticles, where plasmon field enhancements also occur, whereas for larger nanoparticles the SHG signal contains multipolar terms and has been attributed to retardation effects. We can intuitively understand this trend, considering that upon increasing the size of the nanoparticles, the surface-to-volume ratio decreases. At infinity, the nanoparticle size increase leads to the case of a continuous film made of centrosymmetric gold, where the surface and volume SHG terms are indeed attributed to dipolar and quadrupolar contributions, respectively.

1.3. Second Harmonic Generation from Continuous Metal Films. In this subsection, we consider the influence of near-field enhancements on the SHG signal from continuous metal films. In continuous metal films, the SHG source terms are related to the surface and the bulk of the film. While it is intuitively immediately understandable that the surface breaks the symmetry, we could think of the bulk contributions as related to the gradient of electric fields throughout the light-penetration depth. The polarization at the second harmonic frequency can then be written as

$$\begin{aligned} P_i(2\omega) &\propto P_i^D(2\omega) + P_i^Q(2\omega) \\ &= \chi_{ijk} : \mathrm{E}_j(\omega)\, \mathrm{E}_k(\omega) + \chi_{ijkl} : \mathrm{E}_j(\omega) \nabla_k \mathrm{E}_l(\omega) \end{aligned} \quad (4)$$

where χ_{ijk} and χ_{ijkl} are second- and third-rank susceptibility tensors, respectively, and i, j, k, and l represent any of the Cartesian coordinates X, Y, and Z. The coordinate system is oriented so that X and Y are in the plane of the sample, with Y along the direction of S polarization and Z perpendicular to the sample. The first term in eq 4 is the surface-specific electric dipole contribution, as indicated by index D. Within this term, the susceptibility tensor χ_{ijk} contains 27 terms. However, the number of terms is greatly simplified depending on the symmetry of the surface. For instance, in the case of an isotropic surface such as that of an amorphous continuous gold film, there are only three independent tensor components: χ_{ZXX}, χ_{XXZ}, and χ_{ZZZ}. The second term in eq 4 includes the bulk-specific electric quadrupole and magnetic dipole contributions indicated by the index Q. As with the term "multipolar" that was discussed above, please note that, here, the terms "electric quadrupole" and "magnetic dipole" do not designate plasmon modes within Mie theory but instead refer to bulk-specific nonlinear sources. Experimentally, the bulk-specific term in eq 4 can be addressed by canceling the surface contributions, for instance, through periodically stacking thin films, whereby all interfaces interfere destructively.[38] In the bulk-specific susceptibility, the tensor χ_{ijkl} contains 81 elements, which again can be greatly reduced by the symmetry of the material. For instance, in the case of the $m3m$ symmetry group to which the face-centered-cubic crystal structure of gold belongs, there are only four independent tensor components: χ_{XXXX}, χ_{XYYX}, χ_{XXYY}, and χ_{XYXY}. Although eq 4 has only two terms, both of these are tensor products, and manipulating them to show the influence of near-field enhancements requires tensor calculus. This type of calculus is not particularly challenging but is perhaps unfamiliar to the reader, especially in the case of the second term. For this reason, we can express this term using vector calculus:

$$\begin{aligned} \mathbf{P}^Q(2\omega) = {} & (\chi_{XXXX} - \chi_{XYYX} - \chi_{XXYY} - \chi_{XYXY}) \sum_i \hat{e}_i E_i(\omega) \nabla_i E_i(\omega) \\ & + \frac{\chi_{XYXY}}{2} \nabla[\mathbf{E}(\omega)\cdot\mathbf{E}(\omega)] + \chi_{XYYX}[\mathbf{E}(\omega)\cdot\nabla]\mathbf{E}(\omega) \\ & + \chi_{XXYY}\mathbf{E}(\omega)[\nabla\cdot\mathbf{E}(\omega)] \end{aligned} \quad (5)$$

Although at first glance this equation is rather complex, it simplifies considerably when a particular system is considered. For instance, in an isotropic medium such as a sputtered thin film made of gold, $\chi_{XXXX} - \chi_{XYYX} - \chi_{XXYY} - \chi_{XYXY} = 0$ and

dx.doi.org/10.1021/la302485c | Langmuir 2012, 28, 15454−15471

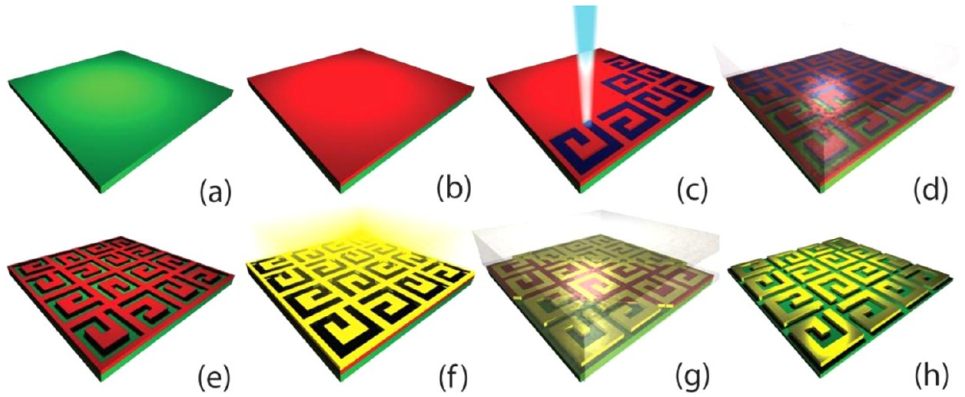

Figure 2. Preparation of a nanostructured plasmonic surface. (a) We start with a Si wafer. (b) A double resist layer is spin-coated on the wafer. (c) Exposure: the nanostructures' pattern is drawn on the resist with electron beam lithography. (d) Development: a solvent removes the resist within the pattern. (e) Drying of the resist produces a mask. (f) The mask is subjected to metal evaporation. (g) Lift-off: all of the resist is removed in a solvent bath. (h) The sample is ready for measurements.

therefore the first term vanishes. This can be easily verified by applying 3-fold and 4-fold symmetry to the χ_{XXXX} tensor component. In a cubic crystalline structure, however, such as a single-crystalline gold film, there is no cancellation and the first term will contribute to the bulk SHG response, depending on the crystal orientation. The second term will be present in most cases, though it vanishes for circularly polarized light. Indeed, for circularly polarized light the scalar product of the electric field with itself is constant and the gradient of a constant is zero. If we consider a single plane wave excitation, the third term is zero because we can write by Fourier transform $\mathcal{F}[\mathbf{E}(\mathbf{r},t)\cdot\nabla](\mathbf{k}, \omega) = [\mathbf{E}(\mathbf{k}, \omega)\cdot i\mathbf{k}]$, which is zero for a transverse electromagnetic wave, with $\mathbf{k}$ being the wave vector of the source polarization. The fourth term is proportional to the total charge density, and it is simply given by Maxwell's equations. Now that we have discussed each individual term, we can introduce the near-field enhancement terms.

If we assume that $\mathbf{E}_{\text{local}}(\omega) = L(\omega)\ \mathbf{E}(\omega)$, where $L(\omega)$ represents the near-field factors for the fundamental frequency and $\mathbf{E}_{\text{local}}(2\omega) = L(2\omega)\ \mathbf{E}(2\omega)$, where $L(2\omega)$ represents the near-field factors at the second harmonic frequency, it then follows through vector calculus that

$$\mathbf{P}_{\text{local}}(2\omega) = L(2\omega)\ L^2(\omega)\ \mathbf{P}(2\omega) \tag{6}$$

Henceforth, the intensity at the second harmonic can be expressed as

$$I(2\omega) \propto |L(2\omega)\ L^2(\omega)\ \mathbf{P}(2\omega)|^2 \tag{7}$$

This relationship implies that, in metal nanostructures, we could expect correspondence between the distribution of local field enhancements at the fundamental frequency and the SHG sources. However, whether there is any SHG signal at all is determined by a consideration of eq 5 and by symmetry arguments. Although symmetry was discussed in relation to the crystallographic unit cell in continuous metal films, the formalism is quite general and can be successfully applied to the symmetry of molecules in molecular films. But what about the symmetry of nanostructures at a nanostructured metal surface?

1.4. Second Harmonic Generation from Nanostructured Metal Surfaces. Nanostructured metal surfaces do not owe all of their optical properties to the nature of the metal involved. Instead, the geometry and arrangement of the nanostructures endow the surfaces with macroscopic properties, which can be quite counterintuitive. For instance, chirality can be a key parameter, as a negative refractive index in artificially structured chiral materials was predicted[39] and reported.[40,41] More generally, because a metal surface can be artificially nanopatterned by methods such as electron beam lithography (EBL, see Figure 2), virtually all possible symmetry arrangements can be studied with second harmonic generation. Of particular importance is the geometry of the surface unit cells, which can be designed to achieve very high near-field enhancements, for example, due to coupling phenomena between nanostructures.

When two plasmonic nanoparticles are placed in close proximity to each other, plasmonic coupling takes place and can lead to SHG enhancements. Such enhancements were reported upon numerically simulating two silver nanorods separated by 28 nm[42] and two gold nanorods separated by 30 nm.[43] Moreover, it was theoretically shown that in coupled plasmonic nanostructures the overall SHG is related to the electromagnetic energy per unit length stored in the gap area between the nanostructures.[44] Experimental work on nanowires has also demonstrated enhanced SHG due to plasmonic coupling between nanostructures.[45,46] In particular, it has been shown that, upon aggregating gold nanoparticles by means of molecular binding, the second harmonic signal is significantly enlarged.[47] Although such an assembly of nanoparticles is random, more ordered configurations have also been studied, such as a regular array of nanocylinders.[48] Besides direct coupling and possible retardation effects, an ordered chain of nanoparticles can support propagating plasmons, a phenomenon that has also been followed by SHG.[49,50] An alternative geometry for studying the interaction of propagating plasmons with nanoparticles consists of using continuous films as a support for the propagating plasmons and employing the nanoparticles as scatterers.[51] Strong local field enhancements are also present at rough surfaces on continuous films, and in these systems, SHG also proves to be a successful probe.[52] The reason for this success is that surface roughness can be regarded as an abundance of symmetry-breaking defects that are localized at the sample surface, and such defects are well-known sources of SHG.[53,54] From defects enhancing the near-field on the surface of a unit cell to macroscopic properties of the nanostructured interface, symmetry sensitivity governs the SHG response. However, because methods such as EBL offer great freedom in designing a surface, a single sample can often

dx.doi.org/10.1021/la302485c | *Langmuir* 2012, 28, 15454−15471

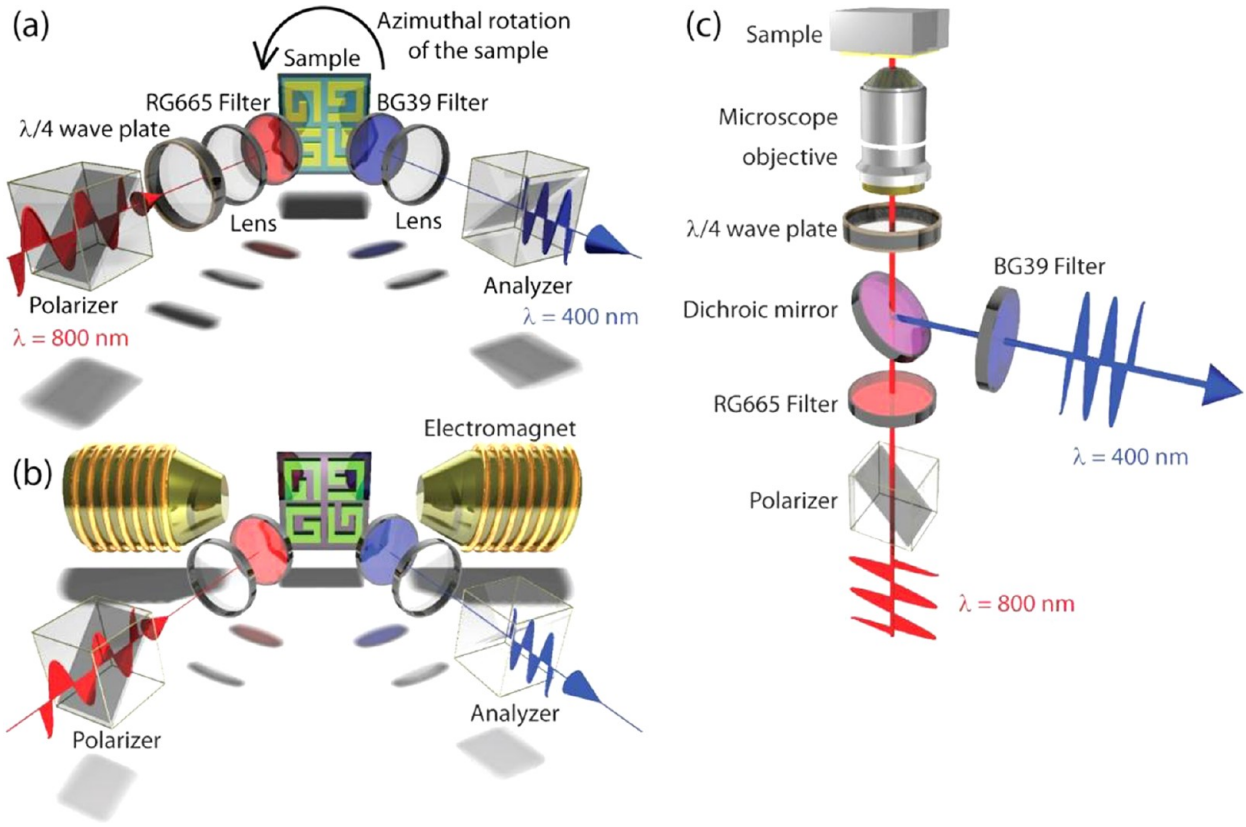

Figure 3. Schematic diagram of the second harmonic generation experiments. (a) Rotating the sample reveals surface symmetry properties. (b) Applying an external magnetic field probes surface/interface magnetization. (c) The microscope configuration shows the surface distribution of second harmonic sources.

exhibit several symmetries simultaneously. How do we distinguish between them in practice?

As we have seen in the previous subsection, the symmetry of the system under study is reflected in the tensor components of the nonlinear susceptibility. According to eq 2, the last two indices of χ_{ijk} relate to the direction of the incident light polarization whereas the first index relates to the direction of light polarization at the second harmonic. It follows that we can address specific tensor components by selecting the orientation of the polarizer and the analyzer in an SHG experiment. Moreover, rotational symmetry can be monitored by mounting the sample on an automatic rotation stage and by following the SHG intensity as a function of the rotational angle (Figure 3a). The symmetry of the sample is then reflected in the symmetry of the recorded SHG pattern. Additionally, chirality is typically investigated by using a quarter-wave plate in order to switch between left- and right-handed circularly polarized incident light. A difference in SHG intensity, depending on the direction of circularly polarized light, is an indication of chirality, especially if that difference reverses upon measuring the mirror image of the sample geometry. Furthermore, time-reversal symmetry breaking is investigated by externally applying a magnetic field to the samples and monitoring the variation in the SHG intensity as a function of the applied magnetic field (Figure 3b). In these experiments, it is considered that magnetization in the sample results from electric current loops; reversing the direction of magnetization is then equivalent to reversing the direction of time, which causes the electric currents to flow backward. Although all of these methods are suitable for examining the macroscopic properties of nanostructured metal surfaces, near-field properties are best studied in a microscopy configuration (Figure 3c).[55−58]

While SHG microscopy can be employed to detect single nanoparticles,[59,60] where the hot spots coincide with the position of the nanostructures, the technique is particularly interesting in the case of ordered arrays, where the pattern of hot spots can differ significantly from that of the underlying geometry, due to coupling and geometric confinement of the near-field. In this case, SHG microscopy allows us to locate the hot spots, to study their origin and to manipulate them. All of these, as well as the resulting macroscopic properties, will be the subject of the following sections. Please note that this Feature Article is not intended to be an exhaustive review of SHG from plasmonic nanostructures. Instead, it is structured as a compilation of useful insights into the dependence of the SHG signal on near-field enhancements, based on direct experience, for the development and possible applications of the technique.

2. LOCATION AND PHYSICAL ORIGIN OF THE SECOND HARMONIC HOT SPOTS

Although studying the macroscopic properties of nanostructured metal surfaces with second harmonic generation (SHG) does not impose any particular restrictions on the samples, studying the near-field enhancements in appreciable detail does. Because the resolution limit of an optical SHG microscope is approximately 200 nm, this value was chosen for both the width of the line and the separation distance of our nanostructures (Figure 4a). The sample was grown on a Si(001) substrate capped with 100-nm-thick SiO_2. A 5-nm-thick

dx.doi.org/10.1021/la302485c | Langmuir 2012, 28, 15454−15471

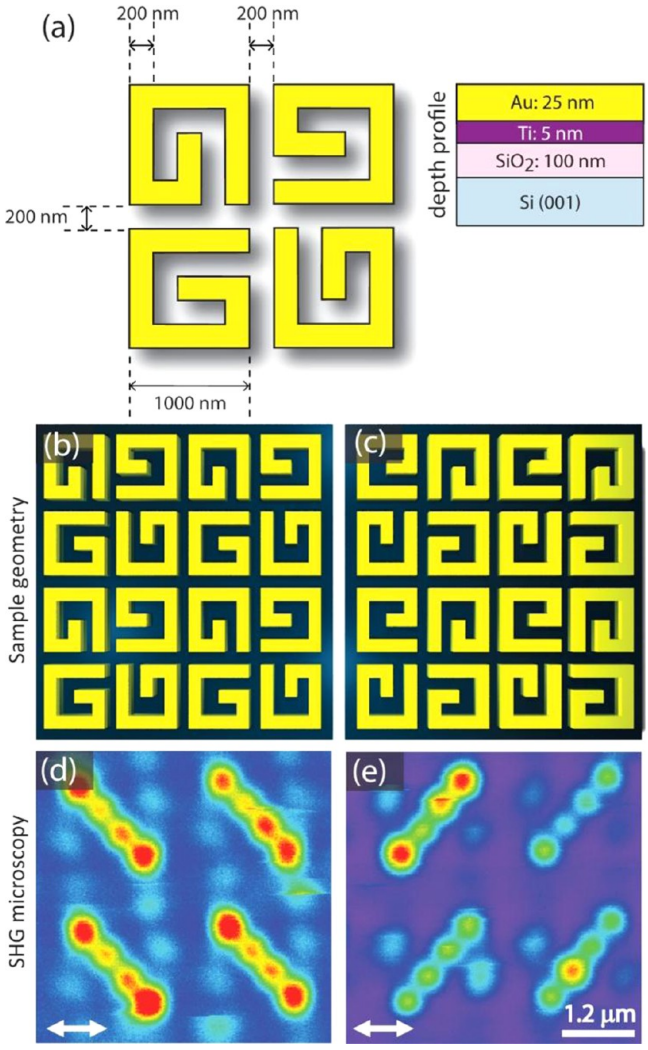

Figure 4. Rather than showing a G-shaped signal, the SHG microscopy reveals a pattern of clearly defined hot spots. (a) The dimensions and depth profile of the nanostructures are presented. The four G-shaped nanostructures are arranged into a unit cell that constitutes the "fruit fly" of our investigations. Schematic diagrams of the (b) G-shaped and (c) mirror-G-shaped periodic arrays. The corresponding SHG microscopy images are shown in (d) and (e), respectively. The white arrows indicate the direction of the linear polarization. The color-coded intensities increase from purple, following the rainbow order of colors.

Ti film served as an adhesion layer for the nanostructures, which were made of 25-nm-thick gold. The gold nanostructures were arranged in periodic arrays, whereby the unit cell consisted of four G-shaped nanostructures, each rotated at 90° with respect to its neighbors (Figure 4b). Additionally, an array of mirror-G-shaped nanostructures was prepared in order to study the effects of chiral symmetry breaking (Figure 4c). The geometry of these G-shaped designs can be resolved with bright-field and dark-field microscopy under white light tungsten halogen illumination. Consequently, it was anticipated that the designs should also be resolved by SHG microscopy.

SHG microscopy was performed with a commercial laser scanning microscope (LSM 510, Zeiss). The light source for this instrument is an ultrafast Ti/sapphire system operated at 800 nm wavelength with a repetition rate of 80 MHz and a pulse width of approximately 200 fs on the microscope stage. The incoming laser pulses are focused with an oil-immersion objective having 100× magnification and a 1.46 numerical aperture. Because of the high numerical aperture for linearly polarized light, the focal spot is elliptical, with the $1/e^2$ waist measuring 330 nm in the polarization direction and 440 nm in the orthogonal direction, whereas for circularly polarized light, a round focal spot with a $1/e^2$ waist of 370 nm is obtained. The second harmonic radiation that is generated in the focal point is separated from the reflected incident light by means of a dichroic mirror and is then directed through an additional color filter before reaching a photomultiplier tube. To form an image, the laser is scanned over the surface of the sample with Galvo mirrors. Typically, images are recorded with a resolution of 512 pixels × 512 pixels, following a two times line averaging and a 102.4 μs pixel dwell time. Interestingly, rather than displaying the expected G-shaped geometry of the samples, the recorded SHG images yielded quite surprising results.

2.1. Highly Localized Sources of Second Harmonic Light: Hot Spots. Figure 4d shows the SHG microscopy results for the array of G-shaped nanostructures. The polarization of incident light is indicated with a white arrow. The color-coded intensities follow the rainbow order, starting with purple for the lowest intensity. More details about the experimental conditions can be found in refs 61 and 62. The figure shows four regions of highly intense second harmonic sources, or hot spots, within each unit cell. More specifically, the four hot spots appear to be situated along the main diagonal of the unit cells. Interestingly, this pattern of hot spots is mirrored upon imaging the array of mirror-G-shaped nanostructures (Figure 4e). The four hot spots themselves are quite large, and that makes it difficult to pinpoint their location on the sample. Determining the precise location of the hot spots is the first step toward understanding their origin.

We have seen that the SHG technique is very sensitive to symmetry. In some complex systems, it can happen that the technique is in fact too sensitive. The challenge then is to identify the main contribution. The nanostructured metal surface in Figure 4 reflects, diffracts, and scatters light. Because of the 3D nature of the nanostructures, there are a large number of interfaces that can interfere constructively and destructively. Additionally, near-field enhancements at the surface of these nanostructures could play an important role. For instance, it is possible that the hot spots originate from electric near-field maxima or perhaps from magnetic near-field maxima, or perhaps still, rather than originating from field maxima, the hot spots might originate from the regions of maximal gradients because gradients also break the centrosymmetry of the material. To understand the role of the near-field enhancements, rigorous numerical simulations were performed.

2.2. Numerical Simulations in the Near-Field Match the SHG Hot Spots. Figure 5a,b shows the SHG microscopy images for the unit cells of G-shaped and mirror-G-shaped gold nanostructures, respectively. To evaluate the role of the near-field enhancements in these unit cells, two independent numerical simulations were performed. First, the electric current in the nanostructures was calculated at 1 nm below the air/gold interface (Figure 5c,d). These calculations were performed with MAGMAS,[63,64] an in-house Maxwell equation solver. Second, the electric near-field was calculated at 1 nm above the air/gold interface (Figure 5e,f). The latter calculations were performed by means of RSoft's DiffractMOD commercial software.[65] Both simulations assumed monochromatic wave excitation at a wavelength of 800 nm and periodic

dx.doi.org/10.1021/la302485c | Langmuir 2012, 28, 15454−15471

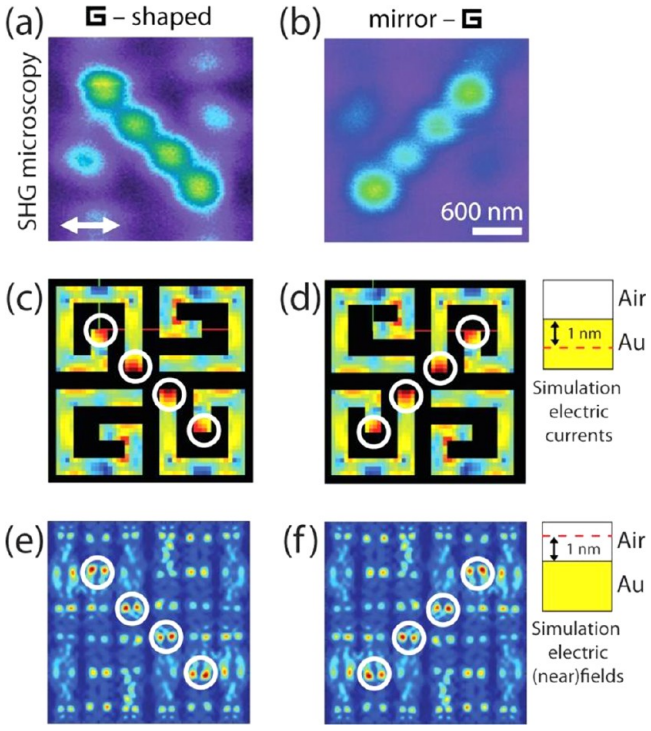

Figure 5. The pattern of experimentally recorded second harmonic hot spots matches the pattern of numerically simulated local field enhancements at the fundamental frequency. (a, b) SHG microscopy (400 nm) from a unit cell of G-shaped and mirror-G-shaped nanostructures, respectively. The direction of light polarization is indicated with a white arrow. (c, d) Corresponding numerical simulations of the electric currents at the fundamental frequency (800 nm), recorded 1 nm below the air/gold interface. (e, f) Numerical simulations of the electric (near-)fields at the fundamental frequency (800 nm) recorded 1 nm above the air/gold interface. The color-coded intensities in all panels follow the rainbow order. In the numerical simulations, the regions of highest intensity have been highlighted with white circles.

boundary conditions, which significantly reduces the simulation time. More details regarding the simulation conditions can be found in ref 66. For all simulation results, the regions of highest intensity are indicated with white circles. It is then clearly apparent that the pattern of second harmonic hot spots matches the pattern of local electric current and electric near-field enhancements at the fundamental wavelength. We can then identify the locations of the SHG hot spots: they are situated at the edges of segments that are perpendicular to the direction of light polarization.

Although the data presented in Figure 5 are unambiguous, they are also unusual. Indeed, we have seen that usually the SHG signal is subject to strict symmetry rules, which causes second harmonic optical responses to be quite different from linear optical responses. It is then fully justified to ask, could the data presented in Figure 5 constitute a mere coincidence? So far, we have compared SHG experimental results and theoretical simulations of the near-fields. To investigate the influence of the near-field on the SHG further, experimental data on the near-field distribution are required as well.

2.3. Experimental Mapping of the Near-Field Matches the SHG Hot Spots. We now turn our attention to nanostructures made of another metal—nickel. Nickel can support near-field enhancements just as gold does; however, the absorption in nickel is much stronger at 800 nm. The larger absorption has important consequences for mapping the regions of near-field enhancements at the nanostructured nickel surface, as we shall soon see.

Figure 6a presents a numerical simulation of the electric currents in the unit cell of G-shaped nanostructures made of

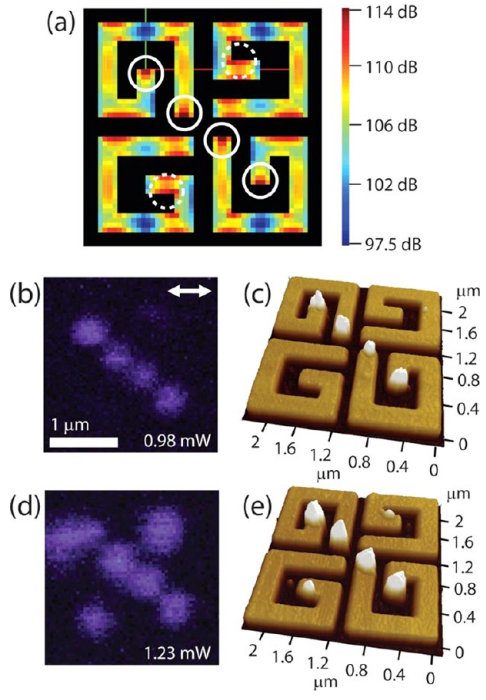

Figure 6. Plasmon-assisted subwavelength laser ablation pinpoints the location of the SHG hot spots. (a) Theoretical simulation of the electric currents in the nickel G-shaped nanostructures. The highest electric field enhancements are indicated with full white circles. The simulation also reveals two regions with a rather high field enhancement, indicated with dashed white circles. (b) The pattern of SHG hot spots obtained for a laser power of 0.98 mW. The white arrow indicates the direction of the incident light polarization. Following illumination, the sample was examined with AFM and the results are shown in (c). Four nanobumps are clearly distinguishable, demonstrating the position of the SHG hot spots on the sample surface. Furthermore, upon increasing the laser power to 1.23 mW, the SHG microscopy also reveals in (d) the enhancements within the dashed white circles in (a). Although these additional hot spots are well resolved in terms of shape and contrast, they are rather large. Consequently, pinpointing their location on the sample surface remains a challenge. However, upon examining the sample after illumination with AFM, in (e), the location of all SHG hot spots is well resolved and corresponds perfectly to the simulation results. These data establish a clear relation between simulations of the near-field at the fundamental frequency, second harmonic emission, and nanoscale shape transformation. This relation suggests a physical mechanism for the origin of SHG from nanostructured surfaces.

nickel. The pattern is rather complex; consequently, for clarity, white circles were drawn to emphasize the most intense hot spots, which are situated along the main diagonal of the unit cell. A similar arrangement of hot spots is clearly visible upon imaging with SHG microscopy, as shown in Figure 6b. Interestingly, following the microscopy experiment, an identical arrangement of hot spots also became clearly visible on the sample surface itself (Figure 6c). The atomic force microscopy (AFM) picture in Figure 6c demonstrates that the SHG hot spots have been imprinted on the sample surface, precisely matching the locations indicated by the numerical simulation.

dx.doi.org/10.1021/la302485c | *Langmuir* 2012, 28, 15454–15471

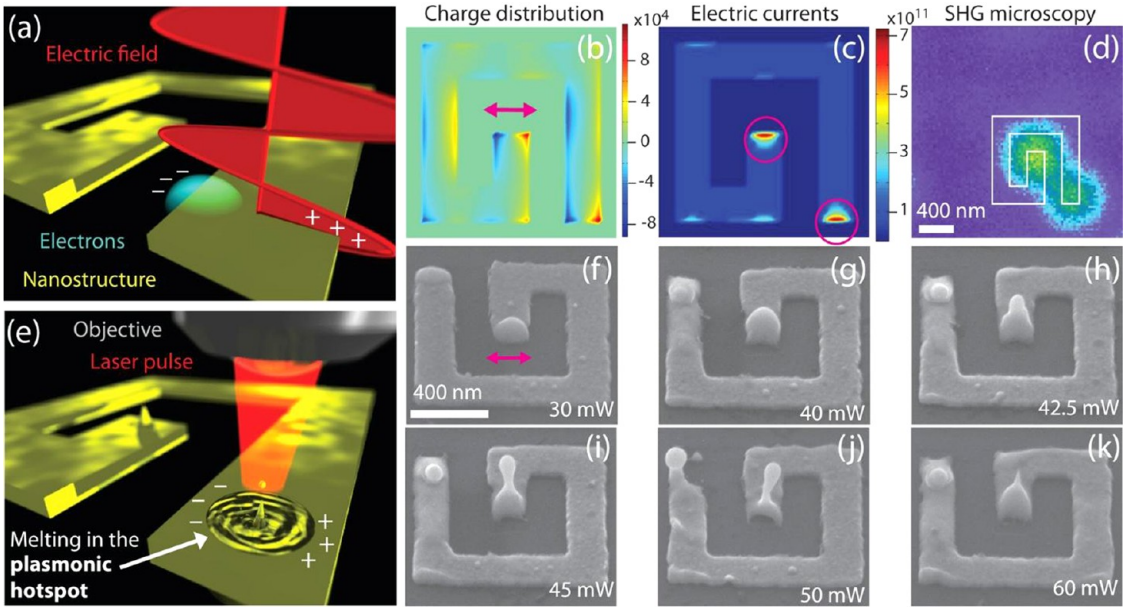

Figure 7. SHG emission occurs as a consequence of light locally driving the electric charges in the nonlinear regime. (a) In response to the incident light's electric field, the electron density oscillates in the plasmonic hot spots. (b) The resulting charge separation is shown by means of a numerical simulation of a G-shaped gold nanostructure. (c) Red circles indicate the location of the highest electric currents associated with the oscillating charges. At low laser intensity, the charges oscillate in the linear regime; when the laser intensity becomes comparable to the local field intensity, the charges oscillate in the nonlinear regime and second harmonic light can be detected, as shown in (d). Furthermore, Ohmic losses that are due to the local electric currents increase the temperature of the material within the plasmonic hot spot above that of the rest of the nanostructure. Consequently, the temperature within the hot spot can increase to above the melting point, and hydrodynamic processes can take place, as represented in (e). A nanobump and back-jet can then be observed precisely in the plasmonic hot spots, whereas for the rest of the nanostructure the temperature remains below the melting point and therefore there are no nanobumps. (f–k) Scanning electron microscopy of the G-shaped gold nanostructures reveals that with increasing laser power a nanobump forms, grows, and results in the formation of back-jets that eject spheres of metal. The direction of light polarization is indicated with the red arrow.

However, this match concerns only the most intense hot spots. What about the rest of the simulation pattern?

Upon further examination of the simulation in Figure 6a, we notice that, besides the four hot spots along the main diagonal, there are two off-diagonal hot spots that are next in intensity and have been highlighted with dashed circles, for clarity. Perhaps they do not contribute to the patterns in Figure 6b,c because they are less intense. If this is so, then the contribution from these off-diagonal hot spots should be revealed upon increasing the incoming laser power. Indeed, whereas in Figure 6b the SHG microscopy was performed with an average power of 0.98 mW, increasing the power to 1.23 mW clearly reveals the off-diagonal hot spots (Figure 6d). The location of these off-diagonal hot spots seems to match that of the simulation results; however, because of the limitations on optical resolution, the SHG hot spots are quite large, making the comparison somewhat difficult. Remarkably though, subsequent imaging with AFM pinpoints the location of the off-diagonal near-field enhancements in excellent agreement with the simulation results. Further increases in the incident laser power imprint even more of the hot spots in Figure 6a, although at the price of great damage in the locations of the four main hot spots. We see therefore that this imprinting constitutes an experimental method for mapping near-field enhancements. It is certainly destructive, but its ease of use, robustness, and high resolution make it very attractive for the fast mapping of near-field enhancements. More details regarding this method can be found in ref 67.

We began this subsection by searching for experimental evidence to corroborate the link between near-field enhancements at the fundamental frequency and SHG emission. We found such evidence in the nanobump surface imprinting. However, this evidence also raises new questions, namely, what is the physical mechanism responsible for the nanobumps and, ultimately, could this mechanism shed light on the link between near-field enhancements of the fundamental frequency and the second harmonic emission?

2.4. Physical Mechanism for the Origin of SHG Hot Spots in Near-Field Enhancements. Modeling a spherical gold nanoparticle as a driven harmonic oscillator (Figure 1b) proves to be very useful in describing plasmon excitations. It also proves very useful in describing second harmonic emission, as we discussed in the Introduction section of this article. We shall now take this model a few steps further and demonstrate that it can provide an explanation of both SHG emission and nanobump formation.

In the driven harmonic oscillator model in Figure 1b, the electric charges on the nanoparticle are driven by the electric field of light. A similar mechanism can be envisioned to take place in the hot spots of a nanostructured gold surface, as illustrated in Figure 7a. It follows that, within these hot spots, the electric field of light can split the charges. The charge separation within the hot spots was verified by numerical simulations performed with MAGMAS (Figure 7b). Moreover, the oscillating charges constitute a local electric current, which is maximal within the hot spots; this local current was also calculated with MAGMAS (Figure 7c). For increasing incident light intensity, this harmonic oscillator enters the nonlinear regime and SHG occurs from the hot spots, as shown in Figure 7d. However, the local electric currents also locally heat up the

dx.doi.org/10.1021/la302485c | *Langmuir* 2012, 28, 15454–15471

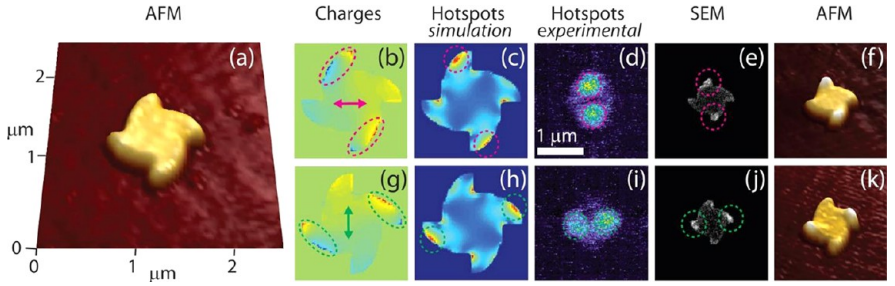

Figure 8. Beyond the G-shaped geometry. (a) AFM image of a star-shaped gold nanostructure before illumination. (b) For horizontally polarized light, a numerical simulation indicating the charge distribution at the surface of the nanostructure is shown. (c) The resulting electric currents are shown. The hot spots were experimentally observed by means of second harmonic generation microscopy, as shown in (d). (e, f) SEM and AFM images show the effects of plasmon-assisted laser ablation. (g–k) On the second row, for vertically polarized light, the images are organized in a similar manner.

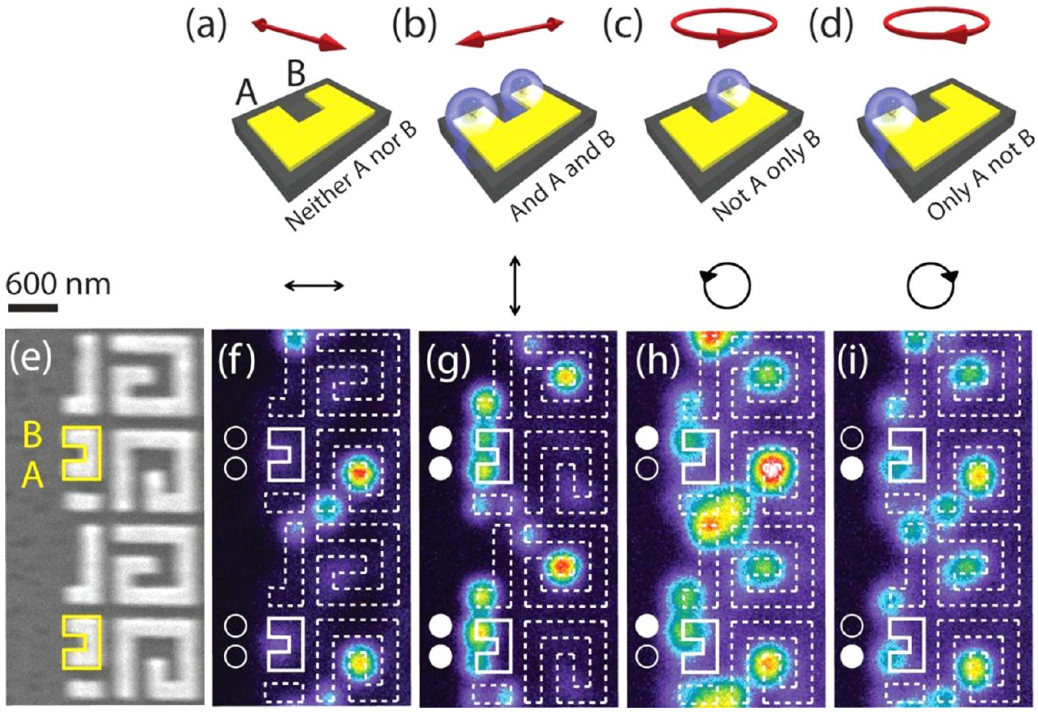

Figure 9. Outputs A and B of a golden U-shaped nanostructure can be either simultaneously on or simultaneously off depending on whether the linearly polarized light is perpendicular or parallel to the nanostructure in (a) and (b), respectively. The outputs can also be switched on individually with circularly polarized light, which is rotated left-handed for B and right-handed for A in (c) and (d), respectively. (e) Scanning electron microscopy (SEM) image of the nanostructures. The U-shaped nanoelement is highlighted in yellow for clarity. Next, SHG microscopy shows the hot spots due to local field enhancements by plasmons for the linearly polarized light, (f) perpendicular and (g) parallel to the U-shaped nanostructures, and for the circularly polarized light, (h) left-handed and (i) right-handed. The color-coded intensities increase from purple through blue, green, yellow, red, and white. The locations of the SHG hot spots are displayed by superposing them on the SEM micrographs. For clarity, the presence or absence of hot spots on the U-shaped nanostructures is indicated by full or empty white circles, respectively.

gold surface, because of the Joule heating effect. If the incident light intensity keeps increasing, this local heating could locally melt the surface within the hot spots. Subsequently, within the hot spots, in response to the impact from intense laser pulses, hydrodynamic processes could take place. These hydrodynamic processes are analogous to the back-jets, which are observed from a surface of water, upon impact from a pebble. As the reader certainly knows, following the impact, a column of water surges upward and often that column ejects a droplet of water. A very similar process can be observed in our gold G-shaped nanostructures, as schematically illustrated in Figure 7e. It is precisely the surging column of molten material that creates the nanobumps in Figure 6c,e. However, in these figures, the nanobumps resulted from the impact of hundreds of light pulses, whereby the response to an individual light pulse is lost. To demonstrate this individual response, illumination was performed with single light pulses with a duration of 60 fs.

In Figure 7f, scanning electron microscopy of the G-shaped gold nanostructures demonstrates that, in response to a single femtosecond pulse, nanobumps can form in the hot spots. As the laser pulse power increases, the nanobumps rise further (Figure 7g) and start forming a column, which is visible in Figure 7h. Further increasing the laser power reveals a nanodroplet shaping up at the end of the column (Figure 7i). In Figure 7j, it can be seen that the nanobumps are hollow. Finally, in Figure 7k, the nanodroplet has flown away, leaving a very sharp cone of gold at the point of detachment. More details about these experiments can be found in ref 68. It

dx.doi.org/10.1021/la302485c | *Langmuir* 2012, 28, 15454–15471

should be noticed that illumination with single femtosecond pulses extended over an area of 6 × 6 μm^2 (i.e. it covered an array of 4 × 4 nanostructures). However, hydrodynamic processes are observed only in the hot spots; the remaining part of the G-shaped nanostructures does not show signs of melting. It is clear, therefore, that the physical mechanism at work is related to the near-field enhancement in the hot spots, but so far, we have considered only G-shaped nanostructures. Is the physical mechanism related to hot spots in general or just to the specific hot spots in G-shaped nanostructures?

Figure 8a presents the AFM micrograph of a 25 nm thick, gold, star-shaped nanostructure before illumination. In Figure 8b, a numerical simulation demonstrates that, under the influence of light's electric field, a charge separation occurs at the vertical tips of the star, highlighted in red dashed line. Correspondingly, local current maxima can be observed in the numerical simulation (Figure 8c). Second harmonic microscopy, in Figure 8d, reveals two clearly distinguishable hot spots whose location seems to match that of the hot spots in the numerical simulations. After illumination, the SEM and AFM micrographs in Figure 8e,f, respectively, confirm that the location of the two nanobumps indeed matches that of the near-field hot spots. A similar match is observed for the vertical polarization, whereby the hot spots are situated on the horizontal edges of the star (Figure 8g–k). Therefore, in star-shaped nanostructures too, visualizing the hot spots as effective "quasi-particles" and evoking the model of the driven harmonic oscillator allow us to understand the SHG emission and the nanobumps intuitively. It seems that this model extends beyond the G-shaped geometry and that it is quite general. However, one of the main reasons for which the model is so intuitively appealing is that it considers linearly polarized light as the cause of an oscillating driving force. It might seem, therefore, that it is limited to linearly polarized excitation. This is not the case, and to demonstrate this, we now turn our attention to circularly polarized light.

2.5. Manipulating the Near-Field and SHG with Circularly Polarized Light. For linearly polarized light, the amplitude of the electric field varies whereas its direction remains constant; for circularly polarized light, the amplitude of the electric field remains constant whereas its direction rotates. Consequently, upon switching the illumination of a nanostructure from linear to circular polarization, the behavior of the electric field of light changes and so does the force on the charges. However, the charges are still driven away from the electric field of light; the latter causes them to oscillate across the nanostructures for linearly polarized light and to rotate around the nanostructure for circularly polarized light. The motion of the charges under circularly polarized light can be illustrated in the case of subwavelength, U-shaped nanostructures.

Figure 9 demonstrates that the two branches (A and B) of a golden U-shaped nanostructure give rise to second harmonic hot spots, which can be selectively switched depending on the polarization state of light. The nanostructure is 600 nm long, 400 nm wide, and 25 nm thick. The line is 200 nm wide. Further details regarding the sample growth and illumination can be found in ref 69. For linearly polarized light, both hot spots can be switched off or on in Figure 9a,b respectively. For circularly polarized light, the hot spots can be switched individually depending on the direction of circular polarization, as indicated in Figure 9c,d. The actual measurements were performed on the sample surface that is illustrated by an SEM image in Figure 9e. For clarity, the U-shaped nanostructures are highlighted in yellow. In the case of horizontally polarized light, the SHG microscopy image in Figure 9f demonstrates that there are no clear hot spots from the U-shaped nanostructures. This absence is emphasized by placing empty white circles in front of branches A and B. Conversely, in the case of vertically polarized light, the SHG micrograph in Figure 9g demonstrates that there are two clear hot spots situated at A and B. The presence of the hot spots is emphasized with full white circles. More importantly though, in the case of circularly polarized light, A and B can be switched individually, as the SHG micrographs in Figure 9h,i demonstrate. One way to a look at this selective switching of hot spots depending on the direction of circularly polarized light is to consider that the polarization rotates the charge density along the achiral U-shaped path. The hot spots could then be explained in terms of accumulated charge density at the end of this particular path. To test this line of reasoning, we will take it a step further and examine the case where there is no end to the path—a ring.

In Figure 10a, we consider ring-shaped gold nanostructures. For linearly polarized illumination, near-field enhancements can be expected and those should give rise to SHG hot spots. For circularly polarized light, though, if the charge density is indeed rotated along the rings, there should be no hot spots. Instead, we can expect the near-field to be distributed over the entire surface of the rings. Numerical simulations of the near-field 1 nm above the gold/air interface are shown in Figure 10b,c for linearly and circularly polarized light, respectively. Additionally, second harmonic microscopy images for linearly and circularly polarized light are shown in Figure 10d,e, respectively. Both the simulations and the microscopy images demonstrate that, for circularly polarized light, the near-field enhancements and the resulting SHG emission are much more homogeneous than for linearly polarized light. These results constitute evidence indicating that the charge density rotates in response to the rotating electric field of circularly polarized light. Moreover, a careful examination of Figure 10c reveals that the near-field pattern is chiral; the handedness of its chirality reverses upon illumination with the opposite direction of circularly polarized light.[70] Because the structure itself is not chiral, the *only* explanation for the presence of chirality in Figure 10c is that the chirality of light has been imparted to the charge distribution (i.e., the charges are responding to the circular motion of the electric field of light).

We have seen that for circularly polarized light the circular motion of the electric field of light is imparted to the charge distribution of nanostructures. Consequently, a nanostructure that is not chiral can acquire a chiral charge distribution. But what about chiral nanostructures? If the charges are indeed rotating because of circularly polarized light, then the chiral geometry of the nanostructure should produce the effect of a ratchet wheel, favoring circular motion along one direction and hampering it along the other. Metal surfaces that are nanostructured with chiral geometry should therefore exhibit very strong circular dichroism effects. To test this idea, we start by considering ratchet-wheel-shaped nanostructures.

3. MACROSCOPIC SECOND HARMONIC SURFACE PROPERTIES

In the previous section, we discussed second harmonic generation from the building blocks of nanostructured metal surfaces. We saw that the polarization of the incident light drives the charge density within single nanostructures, whereby

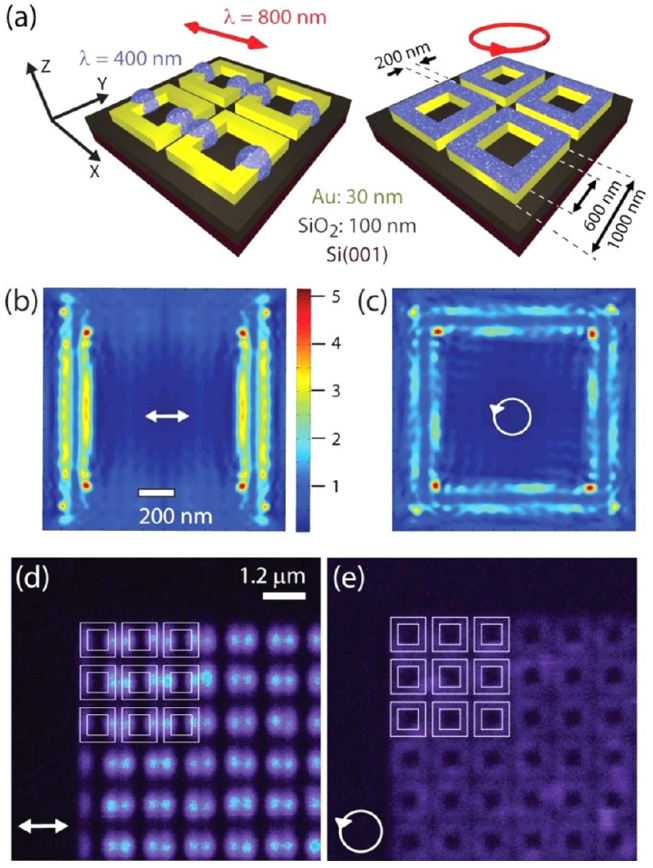

Figure 10. (a) Schematic illustration of the SHG emission from square-ring gold nanostructures depending on the polarization state of light. In response to linearly polarized incident light (red arrow), near-field enhancements of the electric field cause SHG hot spots on the surface. For circularly polarized incident light (red oriented circle), the electric near-field enhancements cause a more homogeneous SHG emission from the surface of the nanostructures. (b, c) Numerical simulations of the electric near-fields in a plane immediately above the air/gold interface. The state of polarization is indicated by white arrows. (d) SHG microscopy pictures for horizontal linearly polarized light revealing hot spots that are arranged along the direction of polarization. (e) SHG microscopy for circularly polarized light shows a homogeneous SHG response from the surface of the square rings.

near-field enhancements can provide the source for the optical nonlinearity, resulting in highly localized SHG emission: hot spots. Consequently, although modern nanopatterning techniques allow us to endow metal surfaces with virtually any possible symmetry, the occurrence of SHG hot spots can effectively reduce the complexity of the nanopatterned surface to a collection of periodically arranged quasi-particles. It follows that a nanopatterned metal surface with a given geometric symmetry might not necessarily display that symmetry in the SHG response. As a rule, understanding the macroscopic SHG response from a nanopatterned metal surface *requires* an understanding of the microscopic response. To illustrate this point, we shall focus on chiral symmetry breaking. In the previous paragraph, we speculated on the interaction of circularly polarized light with ratchet-wheel-shaped nanoparticles; in the next paragraph, we put that speculation to the test.

3.1. Chiral Nanostructured Metal Surfaces with Decoupled Nanoelements. In Figure 11a, atomic force microscopy pictures illustrate the geometry and dimensions of star-shaped nanostructures. The tips of the stars have been curved so that the overall shape resembles a right-handed ratchet wheel. As we have seen while discussing square-ring-shaped nanostructures, upon illumination with circularly polarized light, such a ratchet wheel geometry should favor charge rotation along one direction while hampering charge rotation along the opposite direction. This dependence on the direction of circularly polarized light should be reversed in the case of a left-handed ratchet wheel (Figure 11b). The reversal is clearly visible in the theoretical simulations of the near-field pattern (not shown here, see ref 71) as well as in the experimental SHG microscopy results, which are shown in Figure 11c–f. Indeed, upon illumination with circularly polarized light, the periodic arrays of right- and left-handed star-shaped nanostructures in Figure 11c,d, exhibit a clear difference in SHG intensity—the left-handed stars yield more intensity. In these figures, the direction of circularly polarized light is indicated with an oriented circle. Moreover, upon reversing the direction of circularly polarized light, the difference in SHG intensity, depending on the handedness of the structure, is reversed as well—the right-handed stars yield more intensity (Figure 11e,f).

The second harmonic generation circular dichroism (SHG-CD) in Figure 11c–f illustrates the manner in which the symmetry properties of the nanostructures can be reflected in both the microscopic and the macroscopic SHG responses. However, the macroscopic dependence in this case is a very simple one: it is a direct consequence of summing the microscopic response from the individual building blocks. This case is simple in the sense that the individual building blocks do not influence each other. As we shall see next, when coupling between the nanoparticles occurs, the macroscopic SHG response is far from trivial.

3.2. Chiral Nanostructured Metal Surfaces with Coupled Nanoelements. Let us consider the macroscopic SHG-CD response from three arrangements of chiral nanostructures: G-shaped, mirror-G-shaped, and rearranged. These three are shown respectively in the scanning electron microscopy pictures in Figure 12a–c. For clarity, the borders of the nanostructures have been highlighted in yellow. Because the samples were grown on a nontransparent substrate, the macroscopic SHG-CD can be evaluated in reflection, using the experimental configuration in Figure 3a, and more details on the exact experiment can be found in ref 72. The essential element in Figure 3a is the quarter-wave plate, which is rotated to switch between left- and right-hand circularly polarized light. For every angle of this rotating quarter-wave plate, the SHG intensity can be recorded, and within this record, the chirality appears as a difference in the SHG intensity depending on the direction of circularly polarized light. Figure 12d shows a polar plot of such a record that was obtained from the G-shaped nanostructures. There are four lobes in the figure, oriented along the angles for which the quarter-wave plate produces exactly circularly polarized light. For emphasis, in the figure these angles have been marked with oriented red and green circles. It is immediately apparent that there is a difference between the size of the lobes depending on the direction of circularly polarized light, which is an indication of chirality. The presence of chirality is further confirmed upon measuring the SHG response of the mirror-G-shaped nanostructures, which is presented in Figure 12e. Here again there is a clear difference in lobe size, and compared to the results in Figure 12d, this difference is reversed, exactly as we would expect from chirality.

dx.doi.org/10.1021/la302485c | *Langmuir* 2012, 28, 15454–15471

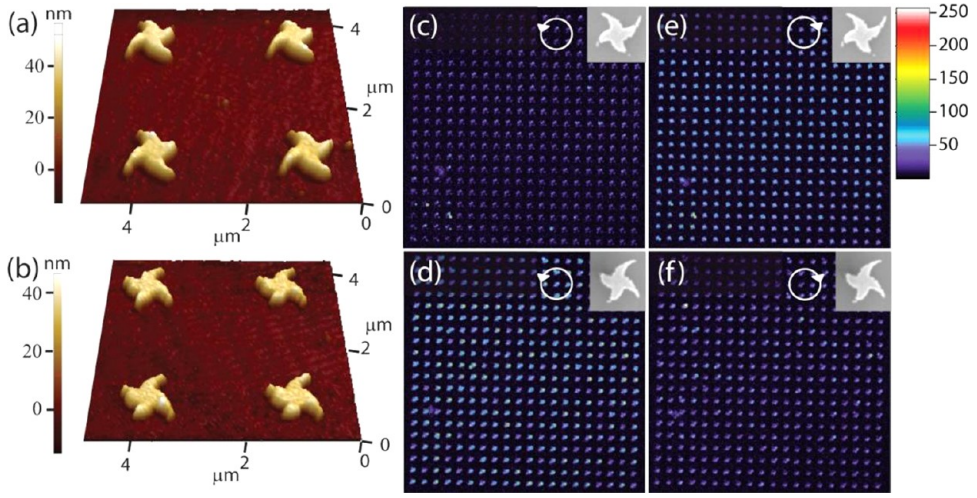

Figure 11. Toward a metamolecular surface: individual nanostructures confer their chiral second harmonic properties to an entire surface. Atomic force microscopy of (a) right-handed and (b) left-handed curved star gold nanostructures. (c, d) SHG microscopy recorded with left-handed circularly polarized light reveals a difference in intensity depending on chirality. As expected, for right-handed circularly polarized light, in (e) and (f) the difference in SHG intensity is reversed. SEM micrographs are shown in the insets.

Quite surprisingly, though, upon measuring the SHG signal from the rearranged nanostructures as a function of the quarter-wave-plate rotation angle, no such difference can be observed. Indeed, all four lobes in Figure 12f appear to have the same size. Consequently, according to the macroscopic SHG signal recorded in Figure 12f, the nanopatterned metal surface in Figure 12c is *not* chiral.

To understand the absence of a chiral signature in the macroscopic SHG response, it is necessary to examine the microscopic SHG emission. Figure 12g–l presents SHG micrographs. The data are organized such that, in each column, the micrographs correspond to the nanostructure arrangement on top of that column, whereas in each row the direction of incident circularly polarized light is identical. It can then be seen that, for the G-shaped nanostructures, the pattern of SHG hot spots differs depending on the direction of circularly polarized light. Additionally, this difference in the hot spot pattern is reversed in the case of the mirror-G-shaped nanoparticles. However, in the case of the rearranged nanoparticles, there is no obvious difference in SHG hot spots, depending on the direction of circularly polarized light. As we have seen in the previous section, the pattern of SHG hot spots can be related to near-field enhancements. Consequently, in the case of G-shaped and mirror-G-shaped nanostructures, the chirality that is observed in the microscopic SHG can be attributed to a chiral near-field coupling between the four Gs at the center of each unit cell. At variance, in the case of the rearranged Gs, the near-field bears no obvious sign of chirality; therefore, no chiral signature can be seen in the macroscopic SHG response.

The data shown in Figure 12 prove that knowing the symmetry of a nanostructured metal surface is insufficient for understanding the macroscopic SHG properties of that surface. In addition, the microscopic SHG emission and the near-field distribution must be taken into account. We have seen that, regarding SHG circular dichroism, both the macroscopic and the microscopic emissions can be studied with the help of a quarter-wave plate. Nanostructured metal surfaces, however, yield other very unusual macroscopic SHG properties, which are much more challenging to understand and require SHG microscopy techniques that are unavailable at the moment.

3.3. Asymmetric Second Harmonic Generation. Figure 13a shows a schematic diagram of a macroscopic SHG property that can be observed from nanostructured gold surfaces: asymmetric SHG. In the experiment, linearly polarized light is incident on the sample, and the detection selects linearly polarized SHG from the sample. The sample itself is rotated azimuthally, and for every angle of sample rotation, the SHG intensity is recorded. Because the sample is 4-fold symmetric, a 4-fold-symmetric SHG response is observed. However, the four peaks themselves are not symmetric. Instead, the polar plot of SHG as a function of the sample rotation angle resembles a ratchet wheel (i.e., it exhibits a sense of rotation). Interestingly, upon measuring the mirror-G-shaped nanostructures, the ratchet wheel of the SHG response seems to rotate in the opposite direction (i.e., the sense of rotation reverses). The actual SHG data can be seen in Figure 13b, where the red curve is associated with the signal from the G-shaped nanostructures and the black one is associated with the signal from the mirror-G-shaped ones. It can clearly be seen that, in each of the four main peaks, the black curve is asymmetric, hence the sense of rotation. At variance, for the red curve, the asymmetry reverses. These data indicate that we can determine the chirality of the nanostructured metal surface through an SHG experiment whereby the sample is rotated. Because these nanostructures are large compared to the wavelength of light, it is likely that, upon sample rotation, their orientation comes to play an important role. However, this effect of the orientation is not always visible (i.e., it is not present in all polarizer–analyzer configurations).

It should be noted that the asymmetric SHG property is not exhibited for arbitrary directions of the polarizer and the analyzer but only for very specific ones (P_{IN}–S_{OUT}). As we have seen earlier, the directions of the polarizer and the analyzer are used to select specific sets of nonlinear susceptibility tensor components. Consequently, this particular macroscopic SHG property is not only due to microscopic SHG sources but, within these microscopic SHG sources, to a specific set of nonlinear susceptibility tensor components. To provide evidence of this origin, a microscopic SHG technique that is capable of discriminating a great number of specific tensor components is required but is currently lacking. The lack is

dx.doi.org/10.1021/la302485c | *Langmuir* 2012, 28, 15454–15471

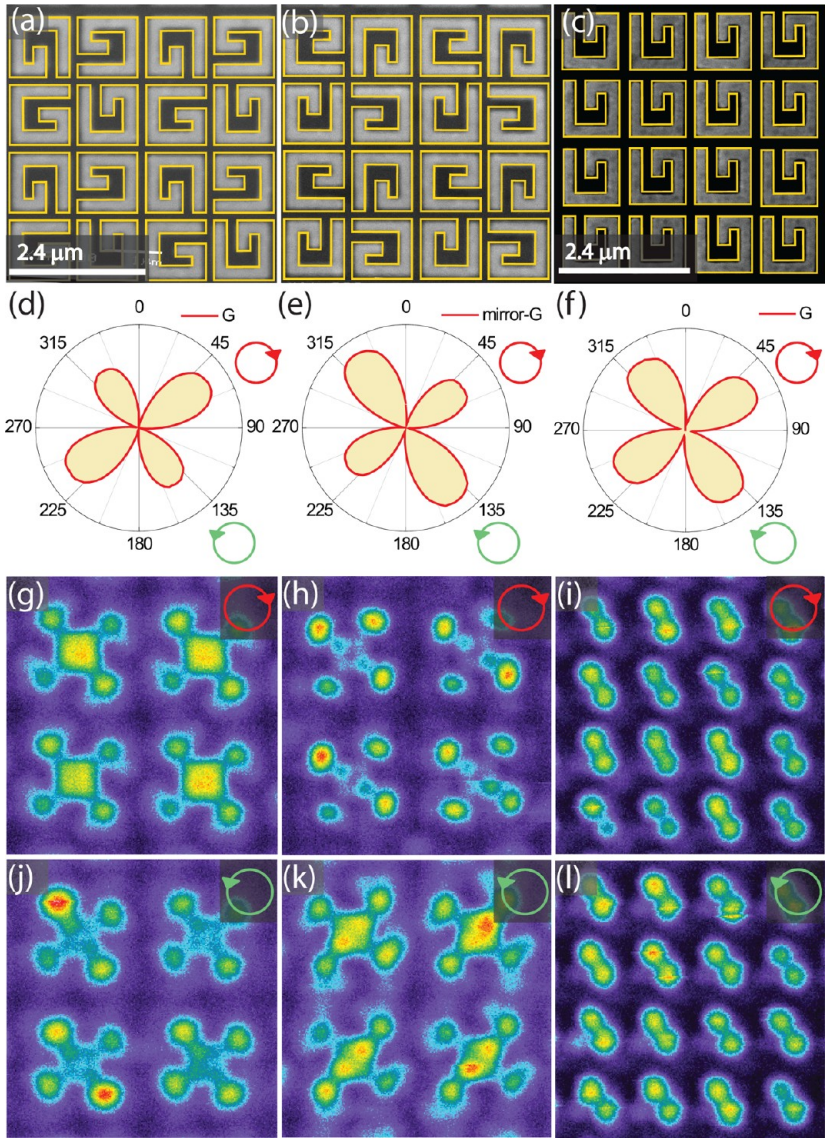

Figure 12. Chirality in the SHG response due to the coupling of four nanostructures. (a–c) SEM pictures of the samples with G-shaped, mirror-G-shape, and rearranged nanostructures, respectively. The yellow lines have been added around the edges of the structures in order to improve the visibility. (d–f) SHG microscopy results obtained for right-handed circularly polarized light corresponding to the SEM pictures. (g–i) SHG microscopy results, obtained for left-handed circularly polarized light. For the G-shaped and the mirror-G-shaped nanostructures, there is a clear difference in the SHG hot spot pattern depending on the direction of circular polarization and on the handedness of the nanostructures. This difference is due to the chiral coupling at the center of the unit cells. For the rearranged nanostructures, no difference in the SHG pattern can be observed depending on the direction of circularly polarized light. (j–l) SHG- circular dichroism results demonstrate that the properties of the hot-spot patterns translate into macroscopic properties of the entire nanostructures surface. The outlined lobes indicate SHG intensity as a function of the angle of quarter-wave plate rotation; the wave plate positions for left- and right-handed circularly polarized light are indicated with oriented circles.

mainly due to technological reasons that should be overcome in the near future. Understanding the asymmetric SHG property constitutes good motivation for such a technological development, and so does the next SHG property that we shall examine, which involves the presence of magnetization.

3.4. Asymmetric-Magnetization-Induced Second Harmonic Generation. The macroscopic SHG property that is schematized in Figure 14a has a lot in common with the above-mentioned asymmetric SHG, and it is just as puzzling. As in the case of Figure 13a, linearly polarized incident light and second harmonic light are involved. As in the case of Figure 13a, the sample is being rotated azimuthally, and as in the case of Figure 13a, the sample consists of G-shaped nanostructures. However, here, instead of being made of gold, the nanostructures are made of nickel. Because nickel is a ferromagnetic material, the direction of its magnetization is controlled with an electromagnet. More details on the sample growth and its magnetic characterization can be found in ref 73. As in the case of Figure 13a, upon rotating the sample, the SHG response exhibits a 4-fold-symmetric pattern with asymmetric peaks. Surprisingly, though, here the asymmetry of the peaks reverses depending on the direction of magnetization within the nanostructures.

The actual SHG data are shown in Figure 14b, where the scale covers the 90° rotation of the sample, which is representative of the full scale because the sample is 4-fold symmetric. While the red dots indicate the magnetization-

dx.doi.org/10.1021/la302485c | *Langmuir* 2012, 28, 15454–15471

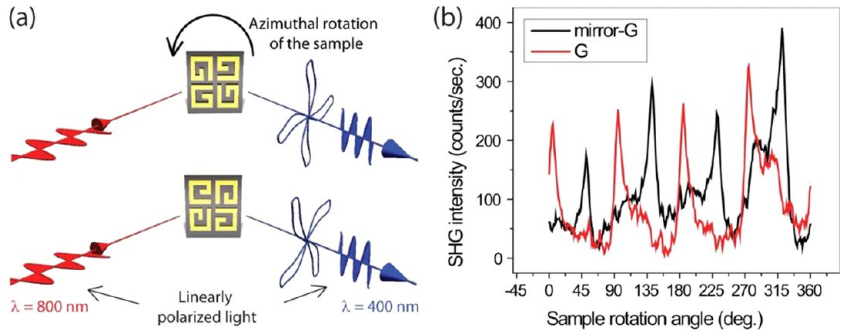

Figure 13. (a) Schematic diagram of asymmetric SHG, a macroscopic property of the nanostructured surface. Upon azimuthal rotation of the sample, for linearly polarized light, the resulting SHG pattern resembles a ratchet wheel with a different sense of rotation and a different phase depending on the handedness. For this experiment, the polarizer was oriented along the horizontal direction whereas the analyzer was positioned along the vertical direction. (b) Actual SHG intensity data as a function of the azimuthal rotational angle of the sample. On each peak, for the mirror-G-shaped nanostructures, the plot shows that the SHG intensity peaks are asymmetric, with the asymmetry reversing for the G-shaped nanostructures, hence the resemblance to a ratchet wheel.

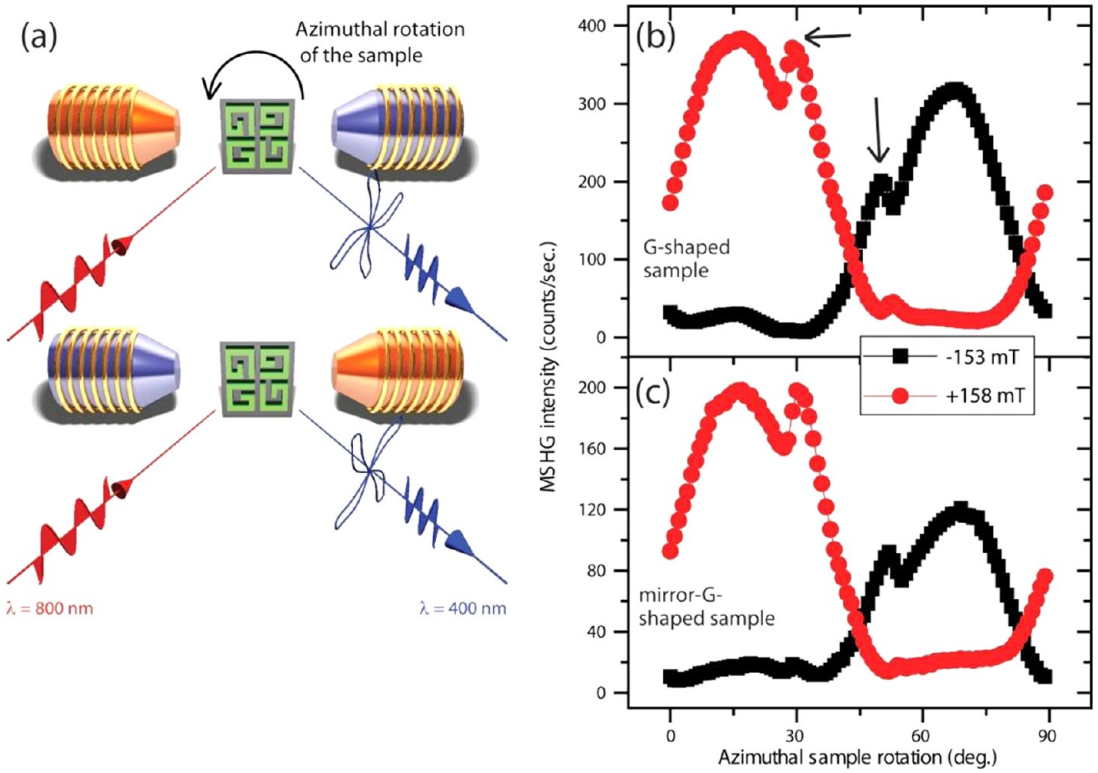

Figure 14. Macroscopic magnetization-induced second harmonic generation property of the G-shaped nickel nanostructured surface. (a) Schematic diagram of the experiment. Upon azimuthal rotation of the sample, in the presence of an externally applied magnetic field and for linearly polarized light, the resulting SHG pattern resembles a ratchet wheel. This wheel has a different sense of rotation and a different phase depending on the sign of the magnetic field. Because the sample is 4-fold symmetric, a rotation from 0 to 90° is representative of the whole angular range. (b) The SHG peak for a positive magnetic field is asymmetric. This asymmetry reverses with the sign of the magnetic field. Interestingly, the asymmetry in these samples is unaffected by chirality as illustrated by the graphs in (c), which correspond to the mirror-G-shaped samples.

induced SHG for an externally applied magnetic field of 158 mT, the black squares indicate the magnetization-induced SHG for an opposite magnetic field: −153 mT. There is clear peak asymmetry in the two SHG signals, which is emphasized with arrows within the figure. Because this asymmetry looks similar to that in Figure 13b, where it is due to chirality, a sample with mirror-G-shaped nickel nanostructures was also measured (Figure 14c). The data in Figure 14c look remarkably similar to those in Figure 14b. Consequently, it seems that chirality does not affect the samples made of nickel; SHG-CD from these samples could not be measured either. It is very puzzling that whereas for gold G-shaped nanostructures the asymmetric SHG constitutes a chiral effect, for nickel G-shaped nanostructures the asymmetric SHG constitutes a magneto-optical one. Clearly, in both cases, the asymmetry is due to the interplay between specific nonlinear susceptibility tensor components. Determining those can be attempted by indentifying the sample symmetries; however, we have seen throughout this article that taking into account the near-field enhancements is absolutely essential.

Asymmetric SHG highlights the necessity for developing new SHG microscopy techniques and suggests that novel SHG

dx.doi.org/10.1021/la302485c | *Langmuir* 2012, 28, 15454−15471

properties remain to be uncovered; for instance, a gold/nickel bilayer might yield a magneto-chitral effect, whereby the asymmetric SHG could be switched both by magnetization and by chirality. It should be noted that all of the data that have been discussed throughout this article were reported in the last 3 years. A similarly fast development can be noted in the output of several other research groups in the field. Consequently, many advances concerning the SHG properties of nanostructured plasmonic surfaces are to be expected in the near future. Extrapolating from the data that have been discussed in this article, in the next section, we shall focus on some of the most promising candidates.

4. SUMMARY AND OUTLOOK

During our investigation of the role of plasmons in SHG from nanostructured metal surfaces, we have seen that the experimental micrographs at the second harmonic match the numerical simulations of the near-field at the fundamental frequency. To explain this observation, we invoked an intuitively appealing model whereby the hot spots constitute quasi-particles whose shape and field anisotropy, combined with intense near-fields, provide the source of the optical nonlinearity and cause local frequency doubling. This model has important implications for mapping plasmonic hot spots at nanostructured metal surfaces. Indeed, at the frequency at which plasmons are excited, reflection, diffraction, scattering, antenna effects, and interferences all contribute to the optical noise from which the near-field signal is to be extracted. Of course, there are elegant and efficient methods for extracting signal from a noisy environment; however, it might be advantageous to avoid the whole problem by detecting the second harmonic light that originates from the plasmonic hot spots. A mere color filter would then be sufficient to improve the signal-to-noise ratio of the experiment dramatically. Compared to other techniques for mapping near-field enhancements in metal nanostructures, such as apertureless scanning near-field optical microscopy,[74] cathodoluminescence,[75] and electron energy loss spectroscopy,[76] the resolution of SHG microscopy is hampered by the diffraction limit of light. However, generally speaking, whereas there are indeed methods to map the plasmonic field enhancements with increasingly high resolution, they come at corresponding increases in cost, measuring time, and complexity. These factors are very important because as a result of the high sensitivity of nanostructured plasmonic surfaces to small variations in geometry, these surfaces are excellent candidates for investigation by the combinatorial discovery approach.[77] In this approach, many slight variations on a desired entity (such as a device or material) are fabricated and then individually characterized to see if they are adequate for the job. The approach has been very successful at finding new drugs and other chemical compounds. In the case of plasmonic nanostructures, arrays of thousands of elements with varying parameters can be prepared and then their individual local field enhancements can be mapped. Obviously, the combinatory discovery approach requires speed and ease of use, which is where the method of SHG microscopy can be of great value. The potential benefits of this method invite future research, especially to determine the limits of its applicability. Because understanding the link between microscopic and macroscopic SHG properties is a key objective, novel methods for microscopy[78] and for analyzing the far-field SHG response[79,80] are necessary.

Taking this model a step further, we have seen that ultrafast laser pulses can cause very intense local currents and heating, melting, and hydrodynamic processes that result in nanobump and nanojet formations in the near-field hot spots. Combined with SHG microscopy, these nanoimprints can further improve our capability to map plasmonic hot spots. Indeed, although visualizing the SHG signal is hampered by the diffraction limit of light, the nanoimprints that light causes can be studied well beyond that limit by means of scanning probe techniques. In addition to providing a technique for mapping the hot spots, these nanoimprints also constitute a writing technique for molding the metal surface. Similarly, whereas the SHG microscope can constitute a tool for visualizing the near-field, it can also serve as a method for manipulating it. We have seen that linearly polarized light has a different effect on the near-field than circularly polarized light. In particular, the latter can induce chirality in the near-field of achiral nanostructures, such as rings. The chiral near-field is even more pronounced when circularly polarized light is incident on chiral nanostructures, such as the G-shaped ones. In the future, this chiral near-field can find important chemical, biological, and pharmaceutical applications in chiral synthesis by providing the means for asymmetric (i.e., enantioselective) catalysis.[81] In turn, materials consisting of a single enantiomer are sought after for their nonlinear optical properties.

Finally, we have seen that unexpected nonlinear optical properties are revealed from nanostructured metal surfaces. For instance, rearranging nanostructures can switch the SHG circular dichroism of the surface. Moreover, upon the azimuthal rotation of a sample whose surface is composed of G-shaped gold nanostructures, an asymmetric SHG response appears, in relation to the chirality of the nanopattern. Additionally, a similar asymmetric SHG response is observed in the case of G-shaped nickel nanostructures, this time in relation to the direction of magnetization. A variety of other such properties can be expected to be uncovered in the future. In every case, we can expect that they will originate in the interplay between symmetry considerations and, especially, the near-field enhancements.

AUTHOR INFORMATION

Corresponding Author

*E-mail: v.k.valev@fys.kuleuven.be. Web site: www.valev.org.

Present Address

[†]Dipartimento di Scienze di Base e Applicate per l'Ingegneria, Sapienza Università di Roma, Via A. Scarpa 16, I-00161 Roma, Italy.

Notes

The authors declare no competing financial interest.

ACKNOWLEDGMENTS

I am grateful to Prof. Thierry Verbiest and Dr. Marco Centini for helpful discussions and for their comments on the text. Financial support from the Fund for Scientific Research Flanders (FWO-V) and from KU Leuven (CREA) is acknowledged.

REFERENCES

(1) Franken, P. A.; Hill, A. H.; Peters, C. W.; Weinreich, G. Generation of optical harmonics. *Phys. Rev. Lett.* **1961**, *7*, 118−119.

(2) Valev, V. K.; Kirilyuk, A.; Rasing, Th.; Dela Longa, F.; Kohlhepp, J. T.; Koopmans, B. Oscillations of the net magnetic moment and

magnetization reversal properties of the Mn/Co interface. *Phys. Rev. B* **2007**, *75*, 012401.
(3) Lee, C. H.; Chang, R. K.; Bloembergen, N. Nonlinear electroreflectance in silicon and silver. *Phys. Rev. Lett.* **1967**, *18*, 167−170.
(4) Kirilyuk, A; Rasing, Th. Magnetization-induced-second-harmonic generation from surfaces and interfaces. *J. Opt. Soc. Am. B* **2005**, *22*, 148−167.
(5) Valev, V. K.; Gruyters, M.; Kirilyuk, A.; Rasing, Th. Influence of quadratic contributions in magnetization-induced second harmonic generation studies of magnetization reversal. *Phys. Status Solidi B* **2005**, *242*, 3027−3031.
(6) Sheng, Y.; Best, A.; Butt, H.-J.; Krolikowski, W.; Arie, A.; Koynov, K. Three-dimensional ferroelectric domain visualization by Čerenkov-type second harmonic generation. *Opt. Express* **2010**, *18*, 16539−16545.
(7) Pavlov, V. V.; Ferré, J.; Meyer, P.; Tessier, G.; Georges, P.; Brun, A.; Beauvillain, P.; Mathet, V. Linear and non-linear magneto-optical studies of Pt/Co/Pt thin films. *J. Phys.: Condens. Matter* **2001**, *13*, 9867−9878.
(8) Byers, J. D.; Yee, H. I.; Hicks, J. M. A second harmonic generation analog of optical rotatory dispersion for the study of chiral monolayers. *J. Chem. Phys.* **1994**, *101*, 6233.
(9) Petralli-Mallow, T.; Wong, T. M.; Byers, J. D.; Yee, H. I.; Hicks, J. M. Circular dichroism spectroscopy at interfaces: a surface second harmonic generation study. *J. Phys. Chem.* **1993**, *97*, 1383−1388.
(10) Maier, S. A. *Plasmonics: Fundamentals and Applications*; Springer: New York, 2007.
(11) Jeanmaire, D. L.; Van Duyne, R. P. Surface Raman spectroelectrochemistry: Part I. Heterocyclic, aromatic, and aliphatic amines adsorbed on the anodized silver electrode. *J. Electroanal. Chem.* **1977**, *84*, 1−20.
(12) Albrecht, M. G.; Creighton, J. A. Anomalously intense Raman spectra of pyridine at a silver electrode. *J. Am. Chem. Soc.* **1977**, *99*, 5215−5217 .
(13) Stockman, M. I. Surface-enhanced Raman scattering: physics and applications. *Top. Appl. Phys.* **2006**, *103*, 47.
(14) Kneipp, K.; Wang, Y.; Kneipp, H.; Perelman, L. T.; Itzkan, I.; Dasari, R. R.; Feld, M. S. Single molecule detection using surface-enhanced Raman scattering (SERS). *Phys. Rev. Lett.* **1997**, *78*, 1667.
(15) Nie, S.; Emory, S. R. Probing single molecules and single nanoparticles by surface-enhanced Raman scattering. *Science* **1997**, *275*, 1102.
(16) Chen, T.; Wang, H.; Chen, G.; Wang, Y.; Feng, Y.; Teo, W. S.; Wu, T.; Chen, H. Hotspot-induced transformation of surface-enhanced Raman scattering fingerprints. *ACS Nano* **2010**, *4*, 3087−3094.
(17) Nitzan, A.; Brus, L. E. Theoretical model for enhanced photochemistry on rough surfaces. *J. Chem. Phys.* **1981**, *75*, 2205−2214.
(18) Chen, C. J.; Osgood, R. M. Direct observation of the local-field-enhanced surface photochemical reactions. *Phys. Rev. Lett.* **1983**, *50*, 1705−1708.
(19) Ueno, K.; Juodkazis, S.; Shibuya, T.; Yokota, Y.; Mizeikis, V.; Sasaki, K.; Misawa, H. Nanoparticle plasmon-assisted two-photon polymerization induced by incoherent excitation source. *J. Am. Chem. Soc.* **2008**, *130*, 6928−6929.
(20) Yokoyama, T.; Masuhara, A.; Onodera, T.; Kasai, H.; Oikawa, H. Plasmon-enhanced photopolymerization of SU-8 on rough gold surfaces. *J. Phys. Chem. C* **2010**, *114*, 19596−19599.
(21) Dostert, K.-H.; Álvarez, M.; Koynov, K.; del Campo, A.; Butt, H.-J.; Kreiter, M. Near field guided chemical nanopatterning. *Langmuir* **2012**, *28*, 3699−3703.
(22) Deeb, C.; Zhou, X.; Gérard, D.; Bouhelier, A.; Jain, P. K.; Plain, J.; Soppera, O.; Royer, P.; Bachelot, R. Off-resonant optical excitation of gold nanorods: nanoscale imprint of polarization surface charge distribution. *J. Phys. Chem. Lett.* **2011**, *2*, 7−11.
(23) Sakellari, I.; Kabouraki, E.; Gray, D.; Purlys, V.; Fotakis, C.; Pikulin, A.; Bityurin, N.; Vamvakaki, M.; Farsari, M. Diffusion-assisted high resolution direct femtosecond laser writing. *ACS Nano* **2012**, *6*, 2302−2311.
(24) Vasilantonakis, N.; Terzaki, K.; Sakellari, I.; Purlys, V.; Gray, D.; Soukoulis, C. M.; Vamvakaki, M.; Kafesaki, M.; Farsari, M. Three-dimensional metallic photonic crystals with optical bandgaps. *Adv. Mater.* **2012**, *24*, 1101−1105.
(25) Dondapati, S. K.; Sau, T. K.; Hrelescu, C.; Klar, T. A.; Stefani, F. D.; Feldmann, J. Label-free biosensing based on single gold nanostars as plasmonic transducers. *ACS Nano* **2010**, *4*, 6318−6322.
(26) Yonzon, C. R.; Jeoung, E.; Zou, S.; Schatz, G. C.; Mrksich, M.; Van Duyne, R. P. A comparative analysis of localized and propagating surface plasmon resonance sensors: the binding of concanavalin a to a monosaccharide functionalized self-assembled monolayer. *J. Am. Chem. Soc.* **2004**, *126*, 12669−12676.
(27) Abid, J. P.; Nappa, J.; Girault, H. H.; Brevet, P. F. Pure surface plasmon resonance enhancement of the first hyperpolarizability of gold core−silver shell nanoparticles. *J. Chem. Phys.* **2004**, *121*, 12577.
(28) Antoine, R.; Péllarin, M.; Prével, B.; Palpant, B.; Broyer, M.; Galletto, P.; Brevet, P. F.; Girault, H. H. Surface plasmon enhanced second harmonic response from gold clusters embedded in an alumina matrix. *J. Appl. Phys.* **1998**, *84*, 4532.
(29) Galletto, P.; Brevet, P. F.; Girault, H. H.; Antoine, R.; Broyer, M. Size dependence of the surface plasmon enhanced second harmonic response of gold colloids: towards a new calibration method. *Chem. Commun.* **1999**, *7*, 581−582.
(30) Russier-Antoine, I.; Nappa, J.; Benichou, E.; Jonin, Ch.; Brevet, P. F. Wavelength dependence of the hyper Rayleigh scattering response from gold nanoparticles. *J. Chem. Phys.* **2004**, *120*, 10748.
(31) Nappa, J.; Russier-Antoine, I.; Benichou, E.; Jonin, Ch.; Brevet, P. F. Wavelength dependance of the retardation effects in silver nanoparticles followed by polarization resolved hyper Rayleigh scattering. *Chem. Phys. Lett.* **2005**, *415*, 246.
(32) Nappa, J.; Revillod, G.; Abid, J. P.; Russier-Antoine, I.; Jonin, Ch.; Benichou, E.; Girault, H. H.; Brevet, P. F. Hyper Rayleigh scattering of gold nanorods and their relationship with linear assemblies of gold nanospheres. *Faraday Disc.* **2004**, *125*, 145 .
(33) Russier-Antoine, I.; Duboisset, J.; Bachelier, G.; Benichou, E.; Jonin, Ch.; Del Fatti, N.; Vallée, F.; Sanchez-Iglesias, A.; Pastoriza-Santos, I.; Liz-Marzan, L. M.; Brevet, P. F. Symmetry cancellations in the quadratic hyperpolarizability of non centrosymmetric gold decahedra. *J. Phys. Chem. Lett.* **2010**, *1*, 874.
(34) Nappa, J.; Revillod, G.; Russier-Antoine, I.; Benichou, E.; Jonin, Ch.; Brevet, P. F. Electric dipole origin of the second harmonic generation from small metallic particles. *Phys. Rev. B* **2005**, *71*, 165407.
(35) Nappa, J.; Russier-Antoine, I.; Benichou, E.; Jonin, Ch.; Brevet, P. F. Second-harmonic light generation from small gold metallic particles: from the dipolar to the quadrupolar response. *J. Chem. Phys.* **2006**, *125*, 184712.
(36) Russier-Antoine, I; Benichou, E.; Bachelier, G.; Jonin, Ch.; Brevet, P. F. Multipolar contributions of the second harmonic generation from silver and gold nanoparticles. *J. Phys. Chem. C* **2007**, *111*, 9044.
(37) Bachelier, G.; Russier-Antoine, I.; Benichou, E.; Jonin, Ch.; Brevet, P. F. Multipolar second harmonic generation in noble metal nanoparticles. *J. Opt. Soc. Am. B* **2008**, *25*, 955.
(38) Larciprete, M. C.; Belardini, A.; Cappeddu, M. G.; de Ceglia, D.; Centini, M.; Fazio, E.; Sibilia, C.; Bloemer, M. J.; Scalora, M. Second-harmonic generation from metallodielectric multilayer photonic-band-gap structures. *Phys. Rev. A* **2008**, *77*, 013809.
(39) Pendry, J. B. A chiral route to negative refraction. *Science* **2004**, *306*, 1353−1355.
(40) Zhang, S.; Park, Y.-S.; Li, J.; Lu, X.; Zhang, W.; Zhang, X. Negative refractive index in chiral metamaterials. *Phys. Rev. Lett.* **2009**, *102*, 23901.
(41) Plum, E.; Zhou, J.; Dong, J.; Fedotov, V. A.; Koschny, T.; Soukoulis, C. M.; Zheludev, N. I. Metamaterial with negative index due to chirality. *Phys. Rev. B* **2009**, *79*, 035407.

(42) Centini, M.; Benedetti, A.; Sibilia, C.; Bertolotti, M. Coupled 2D Ag nano-resonator chains for enhanced and spatially tailored second harmonic generation. *Opt. Express* **2011**, *19*, 8218−8232.
(43) Benedetti, A.; Centini, M.; Bertolotti, M.; Sibilia, C. Second harmonic generation from 3D nanoantennas: on the surface and bulk contributions by far-field pattern analysis. *Opt. Express* **2011**, *19*, 26752.
(44) Benedetti, A.; Centini, M.; Sibilia, C.; Bertolotti, M. Engineering the second harmonic generation pattern from coupled gold nanowires. *J. Opt. Soc. Am. B* **2010**, *27*, 408−416.
(45) Belardini, A.; Larciprete, M. C.; Centini, M.; Fazio, E.; Sibilia, C.; Bertolotti, M.; Toma, A.; Chiappe, D.; Buatier de Mongeot, F. Tailored second harmonic generation from self-organized metal nanowires arrays. *Opt. Express* **2009**, *17*, 3603−3609.
(46) Belardini, A.; Larciprete, M. C.; Centini, M.; Fazio, E.; Sibilia, C.; Chiappe, D.; Martella, C.; Toma, A.; Giordano, M.; Buatier de Mongeot, F. Circular dichroism in the optical second-harmonic emission of curved gold metal nanowires. *Phys. Rev. Lett.* **2011**, *107*, 257401.
(47) Russier-Antoine, I.; Huang, J.; Benichou, E.; Bachelier, G.; Jonin, Ch.; Brevet, P. F. Hyper rayleigh scattering of protein-mediated gold nanoparticles aggregates. *Chem. Phys. Lett.* **2008**, *450*, 345.
(48) Awada, Ch.; Kessi, F.; Jonin, Ch.; Adam, P. M.; Kostcheev, S.; Bachelot, R.; Royer, P.; Russier-Antoine, I.; Benichou, E.; Bachelier, G.; Brevet, P. F. On- and off-axis second harmonic generation from an array of gold metallic nanocylinders. *J. Appl. Phys.* **2011**, *110*, 023109.
(49) Biris, C. G.; Panoiu, N. C. Excitation of dark plasmonic cavity modes via nonlinearly induced dipoles: applications to near-infrared plasmonic sensing. *Nanotechnology* **2011**, *22*, 235502.
(50) Biris, C. G.; Panoiu, N. C. Excitation of linear and nonlinear cavity modes upon interaction of femtosecond pulses with arrays of metallic nanowires. *Appl. Phys. A* **2011**, *103*, 863−867.
(51) Cao, L.; Panoiu, N. C.; Osgood, R. M. Surface second-harmonic generation from surface plasmon waves scattered by metallic nanostructures. *Phys. Rev. B* **2007**, *75*, 205401.
(52) Smolyaninov, I. I.; Zayats, A. V.; Davis, C. C. Near-field second harmonic generation from a rough metal surface. *Phys. Rev. B* **1997**, *56*, 9290−9293.
(53) Zayats, A. V.; Kalkbrenner, T.; Sandoghdar, V.; Mlynek, J. Second-harmonic generation from individual surface defects under local excitation. *Phys. Rev. B* **2000**, *61*, 4545.
(54) Canfield, B. K.; Kujala, S.; Laiho, K.; Jefimovs, K.; Turunen, J.; Kauranen, M. Chirality arising from small defects in gold nanoparticle arrays. *Opt. Express* **2006**, *14*, 950−955.
(55) Zayats, A. V.; Smolyaninov, I. I.; Davis, C. C. Observation of localized plasmonic excitations in thin metal films with near-field second-harmonic microscopy. *Opt. Commun.* **1999**, *169*, 93−96.
(56) Anceau, C.; Brasselet, S.; Zyss, J.; Gadenne, P. Local second-harmonic generation enhancement on gold nanostructures probed by two-photon microscopy. *Opt. Lett.* **2003**, *28*, 713−715.
(57) Berline, I.; Fiorini-Debuisschert, C.; Royal, C.; Douillard, L.; Charra, F. Molecular second harmonic generation induced at a metallic tip. *J. Appl. Phys.* **2008**, *104*, 103113.
(58) Zavelani-Rossi, M.; Celebrano, M.; Biagioni, P.; Polli, D.; Finazzi, M.; Duò, L.; Cerullo, G.; Labardi, M.; Allegrini, M.; Grand, J.; Adam, P.-M. Near-field second-harmonic generation in single gold nanoparticles. *Appl. Phys. Lett.* **2008**, *92*, 093119.
(59) Butet, J.; Duboisset, J.; Bachelier, G.; Russier-Antoine, I.; Benichou, E.; Jonin, C.; Brevet, P. F. Optical second harmonic generation of single metallic nanoparticles embedded in a homogeneous medium. *Nano Lett.* **2010**, *10*,, 1717−1721.
(60) Butet, J.; Bachelier, G.; Duboisset, J.; Bertorelle, F.; Russier-Antoine, I.; Jonin, C.; Benichou, E.; Brevet, P. F. Three-dimensional mapping of single gold nanoparticles embedded in a homogeneous transparent matrix using optical second-harmonic generation. *Opt. Express* **2010**, *18*, 22314−22323.
(61) Valev, V. K.; Silhanek, A. V.; Smisdom, N.; De Clercq, B.; Gillijns, W.; Aktsipetrov, O. A.; Ameloot, M.; Moshchalkov, V. V.; Verbiest, T. Linearly polarized second harmonic generation microscopy reveals chirality. *Opt. Express* **2010**, *18*, 8286−8293.
(62) Valev, V. K.; Silhanek, A. V.; Smisdom, N.; De Clercq, B.; Gillijns, W.; Aktsipetrov, O. A.; Ameloot, M.; Moshchalkov, V. V.; Verbiest, T. Linearly polarized second harmonic generation microscopy reveals chirality: erratum. *Opt. Express* **2011**, *19*, 9242−9244.
(63) Vrancken, M.; Vandenbosch, G. A. E. Hybrid dyadic - mixed potential and combined spectral - space domain integral equation analysis of quasi 3d structures in stratified media. *IEEE Trans. Microwave Theory Tech.* **2003**, *51*, 216−225.
(64) Schols, Y.; Vandenbosch, G. A. E. Separation of horizontal and vertical dependencies in a surface/volume integral equation approach to model quasi 3D structures in multilayered media. *IEEE Trans. Antennas Propag.* **2007**, *55*, 1086−1094.
(65) Diffract MOD, RSoft Design Group. http://www.rsoftdesign.com.
(66) Valev, V. K.; Zheng, X.; Biris, C. G.; Silhanek, A. V.; Volskiy, V.; De Clercq, B.; Aktsipetrov, O. A.; Ameloot, M.; Panoiu, N. C.; Vandenbosch, G. A. E.; Moshchalkov, V. V. The origin of second harmonic generation hotspots in chiral optical metamaterials. *Opt. Mater. Express* **2011**, *1*, 36−45.
(67) Valev, V. K.; Silhanek, A. V.; Jeyaram, Y.; Denkova, D.; De Clercq, B.; Petkov, V.; Zheng, X.; Volskiy, V.; Gillijns, W.; Vandenbosch, G. A. E.; Aktsipetrov, O. A.; Ameloot, M.; Moshchalkov, V. V.; Verbiest, T. Hotspot decorations map plasmonic patterns with the resolution of scanning probe techniques. *Phys. Rev. Lett.* **2011**, *106*, 226803.
(68) Valev, V. K.; Denkova, D.; Zheng, X.; Kuznetsov, A. I.; Reinhardt, C.; Chichkov, B. N.; Tsutsumanova, G.; Osley, E. J.; Petkov, V.; De Clercq, B.; Silhanek, A. V.; Jeyaram, Y.; Volskiy, V.; Warburton, P. A.; Vandenbosch, G. A. E.; Russev, S.; Aktsipetrov, O. A.; Ameloot, M.; Moshchalkov, V. V.; Verbiest, T. Plasmon-enhanced sub-wavelength laser ablation: plasmonic nanojets. *Adv. Mater.* **2012**, *24*, OP29−OP35.
(69) Valev, V. K.; Silhanek, A. V.; De Clercq, B.; Gillijns, W.; Jeyaram, Y.; Zheng, X.; Volskiy, V.; Aktsipetrov, O. A.; Vandenbosch, G. A. E.; Ameloot, M.; Moshchalkov, V. V.; Verbiest, T. U-shaped switches for optical information processing at the nanoscale. *Small* **2011**, *7*, 2573−2576.
(70) Valev, V. K.; De Clercq, B.; Biris, C. G.; Zheng, X.; Denkova, D.; Jeyaram, Y.; Panoiu, N. C.; Silhanek, A. V.; Volskiy, V.; Vandenbosch, G. A. E.; Ameloot, M.; Moshchalkov, V. V.; Verbiest, T. Distributing the optical near field for efficient field-enhancements in nanostructures. *Adv. Mater.* **2012**, in press; DOI: 10.1002/adma.201201151.
(71) Valev, V. K.; De Clercq, B.; Zheng, X.; Denkova, D.; Osley, E. J.; Vandendriessche, S.; Silhanek, A. V.; Volskiy, V.; Warburton, P. A.; Vandenbosch, G. A. E.; Ameloot, M.; Moshchalkov, V. V.; Verbiest, T. The role of chiral local field enhancements below the resolution limit of second harmonic generation microscopy. *Opt. Express* **2012**, *20*, 256−264.
(72) Valev, V. K.; Smisdom, N.; Silhanek, A. V.; De Clercq, B.; Gillijns, W.; Ameloot, M.; Moshchalkov, V. V.; Verbiest, T. Plasmonic ratchet wheels: switching circular dichroism by arranging chiral nanostructures. *Nano Lett.* **2009**, *9*, 3945.
(73) Valev, V. K.; Volodin, A.; Silhanek, A. V.; Gillijns, W.; De Clercq, B.; Jeyaram, Y.; Paddubrouskaya, H.; Biris, C. G.; Panoiu, N. C.; Aktsipetrov, O. A.; Ameloot, M.; Moshchalkov, V. V.; Verbiest, T. Plasmons reveal the direction of magnetization in nickel nanostructures. *ACS Nano* **2011**, *5*, 91−96.
(74) Hillenbrand, R.; Keilmann, F.; Hanarp, P.; Sutherland, D. S.; Aizpurua, J. Coherent imaging of nanoscale plasmon patterns with a carbon nanotube optical probe. *Appl. Phys. Lett.* **2003**, *83*, 368.
(75) Vesseur, E. J. R.; de Waele, R.; Kuttge, M.; Polman, A. Direct observation of plasmonic modes in Au nanowires using high-resolution cathodoluminescence spectroscopy. *Nano Lett.* **2007**, *7*, 2843.
(76) Nelayah, J.; Kociak, M.; Stéphan, O.; Javier García de Abajo, F.; Tencé, M.; Henrard, L.; Taverna, D.; Pastoriza-Santos, I.; Liz-Marzán, L. M.; Coliex, C. Mapping surface plasmons on a single metallic nanoparticle. *Nat. Phys.* **2007**, *3*, 348.

(77) Plum, E.; Tanaka, K.; Chen, W. T.; Fedotov, V. A.; Tsai, D. P.; Zheludev, N. I. A combinatorial approach to metamaterials discovery. *J. Opt.* **2011**, *13*, 055102.
(78) Bautista, G.; Huttunen, M. J.; Mäkitalo, J.; Kontio, J. M.; Simonen, J.; Kauranen, M. Second-harmonic generation imaging of metal nano-objects with cylindrical vector beams. *Nano Lett.* **2012**, *12*, 3207−3212.
(79) Mamonov, E. A.; Murzina, T. V.; Kolmychek, I. A.; Maydykovsky, A. I.; Valev, V. K.; Silhanek, A. V.; Ponizovskaya, E.; Bratkovsky, A.; Verbiest, T.; Moshchalkov, V. V.; Aktsipetrov, O. A. Coherent and incoherent second harmonic generation in planar G-shaped nanostructures. *Opt. Lett.* **2011**, *36*, 3681−3683.
(80) Mamonov, E. A.; Murzina, T. V.; Kolmychek, I. A.; Maydykovsky, A. I.; Valev, V. K.; Silhanek, A. V.; Verbiest, T.; Moshchalkov, V. V.; Aktsipetrov, O. A. Chirality in nonlinear-optical response of planar G-shaped nanostructures. *Opt. Express* **2012**, *20*, 8518−8523.
(81) Inoue, Y.; Ramamurthy, V. *Chiral Photochemistry*; Marcel Dekker: New York, 2004.